



# Properties, sensitivity, and stability of the Southern Hemisphere salinity minimum layer in the UKESM1 model

Ophélie Meuriot<sup>1</sup> · Camille Lique<sup>2</sup> · Yves Plancherel<sup>1</sup>

Received: 24 October 2021 / Accepted: 17 April 2022 / Published online: 12 May 2022  
© The Author(s) 2022

## Abstract

Antarctic Intermediate Water (AAIW) is a water mass originating in the Southern Ocean characterised by its low salinity. The properties of the salinity minimum layer that characterise AAIW in the CMIP6 UKESM1 model and its response to different climate change scenarios are investigated. In UKESM1, the depth of the salinity minimum shoals by 116 m in the SSP5-8.5 run compared to the control run by 2080–2100. The salinity minimum also gets warmer (+1.9 °C) and lighter (−0.4 kg/m<sup>3</sup>) and surface properties where the salinity minimum outcrops warm, freshen and lighten in all scenarios. In spite of these expected changes in properties, the location where the salinity minimum outcrops does not change in any of the future scenarios. The stability of the outcrop location of the salinity minimum is linked to the relative stability of the position of the Antarctic Circumpolar Current (ACC) in UKESM1. The position of the ACC does not follow the maximum wind stress trend, which intensifies and shifts poleward under radiative forcing. Changes in surface buoyancy fluxes in the region are consistent with the changes in hydrographic properties observed at depth on the salinity minimum mentioned above. However, transformation rates at the density corresponding to the salinity minimum outcrop remain constant in all scenarios. Stability in transformation rates at that density is due to the haline and thermal contributions counteracting one another. This analysis identifies two features (outcrop location, transformation rate) associated with the salinity minimum defining AAIW that show remarkable stability in an otherwise changing world. The effect of model resolution and other parameterisations on these findings have yet to be evaluated.

**Keywords** AAIW · UKESM1 · CMIP6 · Southern Ocean

## 1 Introduction

Antarctic Intermediate Water (AAIW) forms in the Southern Ocean; its core can be identified in most of the Southern Hemisphere as a mid-depth salinity minimum located between 500 and 1500 m. AAIW plays a key role in the global overturning circulation by contributing to the

northward return flow from the Southern to the Northern Hemisphere (Schmitz and McCartney 1993). AAIW's relatively fresh flow also contributes to the global water cycle by compensating the imbalance between high latitudes (dominated by low temperatures and precipitation) and low latitudes (dominated by high temperatures and evaporation) (Carmack 2007). AAIW also acts as a buffer against climate change by storing heat (Gille 2003; Schouten and Matano 2006) and anthropogenic CO<sub>2</sub> emissions (Sabine et al. 2004; Panassa et al. 2018). Based on in situ observations, Sabine et al. (2004) have found that AAIW was contributing to up to 1/6th of the anthropogenic CO<sub>2</sub> storage in the ocean up to 1994, and Panassa et al. (2018) suggested that the storage of anthropogenic CO<sub>2</sub> at depth within AAIW has been increasing over the past decades.

Understanding how AAIW properties will evolve under climate change is crucial to assess the impact on the overturning circulation and storage of heat and anthropogenic CO<sub>2</sub>. Simulations from the Coupled Model Intercomparison

✉ Ophélie Meuriot  
ophelie.meuriot14@imperial.ac.uk

Camille Lique  
camille.lique@ifremer.fr

Yves Plancherel  
y.plancherel@imperial.ac.uk

<sup>1</sup> Earth Science and Engineering, Imperial College London, London, UK

<sup>2</sup> Univ. Brest, CNRS, IRD, Ifremer, Laboratoire d'Océanographie Physique et Spatiale (LOPS), IUEM, Brest 29280, France

Project phase 5 (CMIP5) suggest that most of the water masses in the Southern Ocean tend to lighten and warm in response to an increase in greenhouse gas emissions in the atmosphere, with the largest changes expected for mode and intermediate waters (Sallée et al. 2013a, b). The multi-model mean in Sallée et al. (2013a, b), which includes 21 CMIP5 models, shows that intermediate waters in the Southern Ocean warm by 1.4 °C, freshen by 0.1psu and lighten by 0.3 kg/m<sup>3</sup> by the end of the century in simulations forced with the Representative Concentration Pathway 8.5 (RCP8.5) scenario.

The intermediate depths also present the largest biases in the CMIP5 historical simulations, with mode and intermediate waters in the Southern Ocean lighter and warmer than observations (Sallée et al. 2013a, b; Zhu et al. 2018). Sallée et al. (2013a, b) found that water masses at intermediate depths are on average 1.7 °C warmer and 0.2 kg/m<sup>3</sup> lighter compared to the observation based on a multi model mean, while the salinity biases are smaller. In previous CMIP models, AAIW does not extend as far north compared to observations, with 8 CMIP3 models showing a reduced northward extent in the eastern Pacific Ocean and eastern Indian Ocean (Sloyan and Kamenskovich 2007) and 11 CMIP5 models showing a reduced northward extent in the Atlantic Ocean (Zhu et al. 2018). It remains to be investigated if such biases are still present in the newly available CMIP6 simulations or if the model improvements made between CMIP5 to CMIP6 have affected the way AAIW are resolved and simulated.

Biases found at the intermediate depths in climate models highlight the need to better understand AAIW processes. For instance, the formation mechanisms of AAIW themselves remain unclear, with theories ranging from circumpolar processes with Ekman transport causing water masses to sink all around the Antarctic Circumpolar Current (ACC) between the Antarctic Polar Front (APF) and the Subantarctic Front (SAF) (Deacon 1937) to more localised processes where AAIW forms in the southeast Pacific and the southwest Atlantic through mixing with the densest type of Subantarctic Mode Water (Talley 1999). Talley (1999) identifies AAIW formation areas in the southeast Pacific and southwest Atlantic by analysing the distribution of oxygen, potential vorticity and salinity on the AAIW isopycnals and found that the formation mechanisms were localised rather than occurring at all longitudes. Some studies have further suggested that the formation of AAIW could actually result from a combination of both mechanisms (Sloyan and Rintoul 2001; Yao et al. 2017), although the relative contribution of the two mechanisms remain unknown. It is also likely that formation mechanisms and their relative importance differ from model to model.

The definition itself of AAIW varies in the literature. Although AAIW can be clearly identified by its salinity minimum, there is no consensus on whether the salinity

minimum corresponds to the core of the layer or to its deeper boundary. In addition, the southernmost extent of the salinity minimum has been shown to be closely related to frontal locations such as the Subantarctic Front (SAF) (Pollard et al. 2002; Treguier et al. 2007). In the literature, the distinction between mode and intermediate waters is often omitted, with studies analysing both water masses jointly (Piola and Gordon 1989; Panassa et al. 2018) while other studies combine AAIW with the deeper Upper Circumpolar Deep Water (uCDW) (You 2002). Providing analyses specific to AAIW with a clear definition of the water mass is therefore needed.

Previous investigations of AAIW based on CMIP-type climate models often consider only the zonal average across the Southern Hemisphere (Sallée et al. 2013a, b), or have focused on a specific area (Zhu et al. 2018). It is clear from observations, however, that the distributions and properties of AAIW show zonal heterogeneity between basins, with a lighter and fresher AAIW type in the Pacific and denser and saltier AAIW types in the Indian and Atlantic oceans (Talley et al. 2011), which suggests that both the spatial and temporal variability of AAIW need to be investigated.

The aim of this study is to analyse AAIW properties in one CMIP6 model, the UKESM1-0-LL model from the Met Office Hadley Centre, and to analyse the variability of the salinity minimum in the different basins in order to provide a broader picture of the response of the salinity minimum under future scenarios. The study is structured as follows: Section 2 presents the methods and datasets used. Section 3 describes the definition used to analyse AAIW properties consistently in different scenarios and basins and assesses the link between the salinity minimum and frontal locations. Section 4 evaluates the ability of UKESM1 to represent AAIW properties by comparing the results of the historical UKESM1 simulation to the MIMOC climatology. Section 5 assesses the response of AAIW in future scenarios. Section 6 focuses on the Southern Ocean mechanisms such as wind stress and air-sea fluxes to investigate the possible origins of changes presented in Sect. 5.

## 2 Methods and datasets

### 2.1 CMIP6 UKESM1 model

The data used in this paper comes from simulations performed with the UK Earth System Model 1 low atmosphere and low ocean resolution (UKESM1-0-LL) from the Met Office Hadley Centre (MOHC). A full description of the model can be found in Sellar et al. (2019). Briefly, UKESM1-0-LL is an updated version of the CMIP5 HadGEM2-ES model. UKESM1 is built on multiple component models including HadGEM3-C3.1 for the physical core atmosphere–land–ocean–sea ice model, Joint

UK Land Environment Simulator (JULES) for the terrestrial biogeochemistry component, the Model of Ecosystem Dynamics nutrient Utilisation Sequestration and Acidification (MEDUSA) for the ocean biogeochemistry and United Kingdom Chemistry and Aerosol (UKCA) model for the atmospheric composition. HadGEM3-C3.1 uses the Nucleus for European Modelling of the Ocean (NEMO) model for the ocean and CICE for sea ice (Williams et al. 2018). UKESM1 is run with a  $1^\circ$  latitudinal resolution, enhanced to  $1/3^\circ$  near the equator,  $1^\circ$  longitudinal ocean resolution and a 135 km atmosphere resolution. The ocean grid in the model has 75 unevenly-spaced vertical levels compared to 40 in the CMIP5 HadGEM2-ES. The additional vertical levels yield improved representation of water mass properties in intermediate and deep ocean layers. For the ocean component, parameterisations include a Laplacian horizontal viscosity of  $20,000 \text{ m}^2/\text{s}$  and an isopycnal diffusion coefficient equal to  $1000 \text{ m}^2/\text{s}$  (Kuhlbrodt et al. 2018). Eddies are parametrised based on the Gent et al. (1995) mixing scheme with a spatially varying coefficient based on Held and Larichev (1996). The turbulent kinetic energy (TKE) field is set at a few choke points at the ocean bottom and follows Gaspar et al. (1990) for the TKE parametrisation below the mixed layer.

The simulations used in the present analysis include the piControl and historical runs from the Diagnostic, Evaluation and Characterization of Klima (DECK) experiments which are common to all CMIP phases, and the simulations from the Scenario Model Intercomparison Project (ScenarioMIP) which are specific to CMIP6 (Eyring et al. 2016). The piControl run is initialised from a 500-year coupled spin-up prior to which a 5000-year ocean only simulation and a 1000-year land only simulation were run (Sellar et al. 2019).

The ScenarioMIP correspond to the different shared socioeconomic pathways (SSP). Simulations SSP1-1.9, SSP1-2.6, SSP2-4.5, SSP3-7.0, SSP5-3.4-over and SSP5-8.5 simulations are considered here. The number after the hyphen corresponds to the 2100 forcing level ( $\text{Wm}^{-2}$ ) and the number before corresponds to the category of SSP with SSP1 corresponding to sustainability, SSP2 to middle of the road, SSP3 to regional rivalry, SSP4 to inequality and SSP5 to fossil fuel development (O'Neill et al. 2016). The increase of the mean atmospheric temperature is expected to reach  $5^\circ\text{C}$  by 2100 under the SSP5-8.5 scenario and  $3^\circ\text{C}$  under the SSP2-4.5-over. In the SSP5-3.4-over scenario, carbon emissions increase at the same rate as in the SSP5-8.5 scenario until 2040 and then decrease to negative carbon emissions from 2070 onward. Full details can be found in O'Neill et al. (2016).

The historical run is averaged between 1992 and 2014 and compared with the climatological fields from MIMOC (Sect. 4). The piControl and ScenarioMIP simulations are

averaged over the 2080–2100 period to assess the response of the salinity minimum under radiative forcing. Analysing the output of all future scenarios instead of only the most extreme scenario enables us to study the sensitivity of the model to different radiative forcing cases.

## 2.2 MIMOC ocean climatology

MIMOC (Monthly Isopycnal Mixed-Layer Ocean Climatology) consists of optimally interpolated in situ observations mainly from in situ ship CTD profiles and Argo float data. The fields are provided monthly at a  $0.5^\circ \times 0.5^\circ$  resolution from  $80^\circ\text{S}$  to  $90^\circ\text{N}$  and includes potential temperature, practical salinity and pressure as well as mixed-layer depth fields. There are 81 levels ranging from 0 to 1950 dbar. Full details on MIMOC can be found in Schmidt et al. (2013).

## 2.3 Transformation and formation rates

Water mass transformation and formation rates are obtained by following the thermodynamic approach first introduced by Walin (1982) and refined by Speer and Tziperman (1992) to include the effect of salinity. At high latitudes, water masses are ventilated as they outcrop to the surface. Air-sea fluxes modify the surface density through freshwater and heat fluxes. When neglecting the role of mixing in the interior, the transformation rates of the different water masses can be solely derived from the air-sea fluxes at the surface. The surface density flux  $D_{\text{in}}$  is defined as (adapted from Howe and Czaja 2009):

$$D_{\text{in}} = \frac{-\alpha H_{\text{net}}}{C_p} - \beta \times \text{SSS} \times F_{\text{wf}}$$

where  $\alpha$  and  $\beta$  are the thermal and haline expansion coefficients respectively,  $H_{\text{net}}$  is the net heat flux into the ocean,  $F_{\text{wf}}$  the freshwater flux into the ocean which includes precipitation minus evaporation, plus sea ice melt and runoff,  $C_p$  the specific heat and SSS the sea surface salinity. The first term,  $-\alpha H_{\text{net}}/C_p$ , corresponds to the thermal contribution and the second term,  $-\beta \times \text{SSS} \times F_{\text{wf}}$ , to the haline contribution to the density flux.

The transformation rate is obtained by integrating the surface density flux  $D_{\text{in}}$  over the outcrop area of a density range  $\Delta\rho$  and over the time period  $Nt$ . It is divided by  $Nt$  to obtain an average rate.

$$F(\rho) = \frac{1}{\Delta\rho Nt} \int_0^{Nt} \int_{\text{outcrop } \rho}^{\text{outcrop } \rho + \Delta\rho} D_{\text{in}} \, dA \, dt$$

The transformation rate is here calculated with a density bin of  $\Delta\rho=0.1\text{ kg/m}^3$  (similarly to Howe and Czaja 2009) and a time step of a month over a time period of 20 years for the piControl and ScenarioMIP simulations and 22 years for the historical run. The formation rate is taken as the negative of the derivative with respect to density  $-dF/d\rho$ .

### 3 Definitions of the different properties

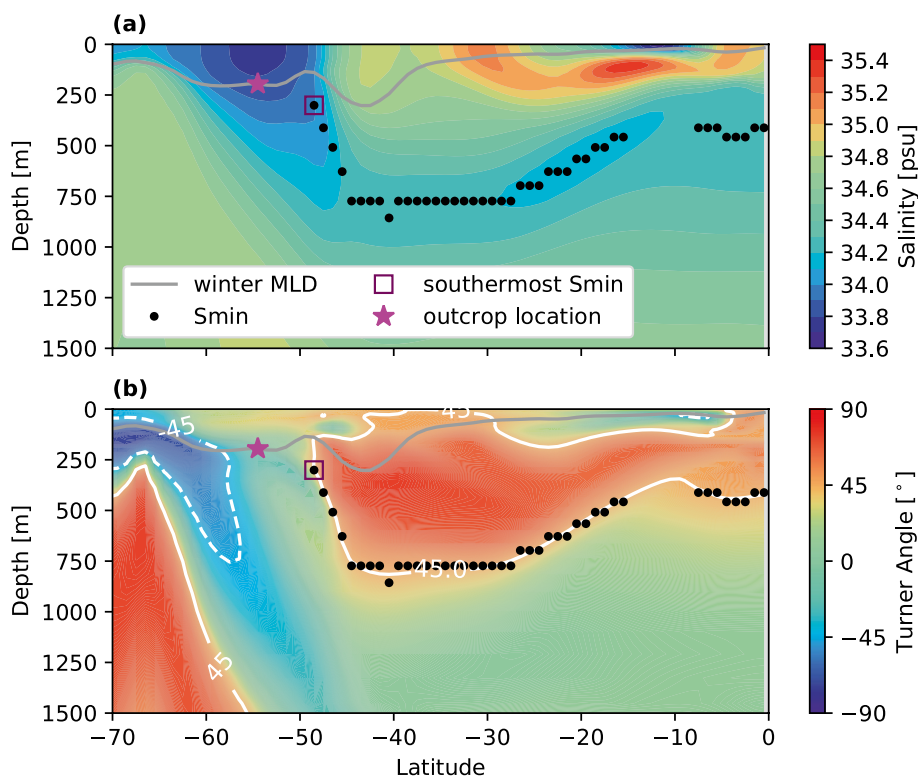
#### 3.1 Salinity minimum

Multiple definitions of AAIW can be found in the literature (Sloyan and Rintoul 2001; Sørensen et al. 2001; McCarthy et al. 2012; Downes et al. 2017; Portela et al. 2020). Some studies define AAIW as a layer bounded by neutral density values (Sloyan and Rintoul 2001; You 2002) or potential density values (Sørensen et al. 2001; Downes et al. 2017; Portela et al. 2020). In contrast, McCarthy et al. (2012) identify AAIW by defining the core of the layer as the depth of the salinity minimum. The salinity minimum definition has the benefit of being consistent across basins and models, in contrast to density classes which vary between basin and model. Downes et al. (2017) choose different density classes for AAIW in each basin and experiment to address that issue, but since density definitions vary between experiments due to different forcing, the salinity

minimum criterion is better suited here as it provides a consistent definition for all experiments. Using the salinity minimum to define AAIW is appropriate here since the aims of this study are to both analyse model results from different scenarios in UKESM1 and compare UKESM1 to MIMOC across the Atlantic, Indian and Pacific basins.

The salinity minimum is defined here as the salinity at the depth where the salinity reaches its minimum between the winter mixed layer depth (calculated as the September mixed layer depth) and 2000 m. The 2000 m limit was chosen based on observational data, 2000 m being deeper than the salinity minimum. September corresponds to the month when the mixed layer is the deepest. Setting the upper limit as the wintertime mixed layer depth provides a suitable way to exclude seasonal surface signals or low salinity signals due to localised areas with high precipitation or ice melt. The depth of the salinity minimum, together with the salinity, temperature and density on the salinity minimum are evaluated in this study. Values corresponding to locations where the salinity minimum depth is equal to the upper or lower limits (the winter mixed layer depth and 2000 m respectively) are removed as they represent areas where no mid-depth salinity minimum is present. The depth of the detected salinity minimum is shown in black for a meridional section across the Pacific Ocean, together with the winter mixed layer depth shown in grey (Fig. 1a). It is located at the centre of the low salinity layer. The southernmost salinity minimum detected

**Fig. 1** Meridional section showing **a** Salinity and **b** Turner angle at  $190^\circ$  (Pacific Ocean) for the UKESM1 historical 1992–2014 averaged period. The full (dashed) white contour line corresponds to a Turner angle value of  $45^\circ$  ( $-45^\circ$ ). The black dots represent the depth of the salinity minimum (detected between the base of the winter mixed layer and 2000 m) with the southernmost salinity minimum indicated by the purple square. The pink stars correspond to the outcrop location of the salinity minimum defined as the meridional salinity minimum at the winter mixed layer depth



is at 48° S (purple square). Between 48°S and 45°S, the salinity minimum gets deeper (from 300 to 800 m) and then remains at a relatively constant depth between 45° S and 28° S. It then shoals as it gets closer to the equator.

### 3.2 Stratification and fronts

The salinity minimum has a physical meaning in terms of stratification. The relation between stratification and temperature and salinity extrema is here investigated through the analysis of the Turner angle, as it provides a useful way to illustrate the role of the salinity minimum with regards to stratification. The Turner angle is defined as  $Tu = \arctan(\alpha T_z - \beta S_z, \alpha T_z + \beta S_z)$ , where  $T_z$  and  $S_z$  are the vertical temperature and salinity gradients, respectively. Figure 1b shows a section of the Turner angle in the Pacific Ocean (190°). High Turner angle values ( $45^\circ < Tu < 90^\circ$ ) correspond to areas where density (and hence stratification) is dominated by temperature and low Turner angle values ( $-45^\circ < Tu < -90^\circ$ ) correspond to areas where stratification is dominated by salinity. For Turner angle values between  $-45^\circ$  and  $45^\circ$ , both salinity and temperature contribute to the determination of density. By definition, temperature and salinity minima correspond to vertical gradients of zero and thus correspond to Turner angle values of  $-45^\circ$  and  $45^\circ$  respectively (indicated as dashed and full white lines in Fig. 1b). It can be seen that the salinity minimum (black dots) and the  $45^\circ$  Turner angle contour line (full white line) coincide. The salinity minimum therefore marks the limit where stratification ceases to be solely dominated by temperature and where both salinity and temperature contribute to stratification. The differences in stratification above and below the salinity minimum suggest that the layers below and above the salinity minimum may present different origins. Indeed, Talley et al. (2011) suggest the formation mechanisms above and beneath the AAIW salinity minimum could be different with localised formation areas in the upper layer (such as subduction in the southeast Pacific) and formation through Ekman transport for the lower layer.

The concept of temperature and salinity contributions to stratification and temperature and salinity minima have been used previously to identify key frontal locations in the Southern Ocean (Orsi et al. 1995; Pollard et al. 2002; Treguier et al. 2007). Pollard et al. (2002) and Treguier et al. (2007) associate the southernmost salinity minimum to the location where temperature ceases to dominate stratification over salinity and refer to it as the Subantarctic Front (SAF). Similarly, they associate the northernmost location where a mid-depth temperature minimum can be found to the Polar Front (PF).

The location of the southernmost salinity minimum is shown in white for both UKESM1 and MIMOC in Fig. 2. The position of the southernmost salinity minimum in

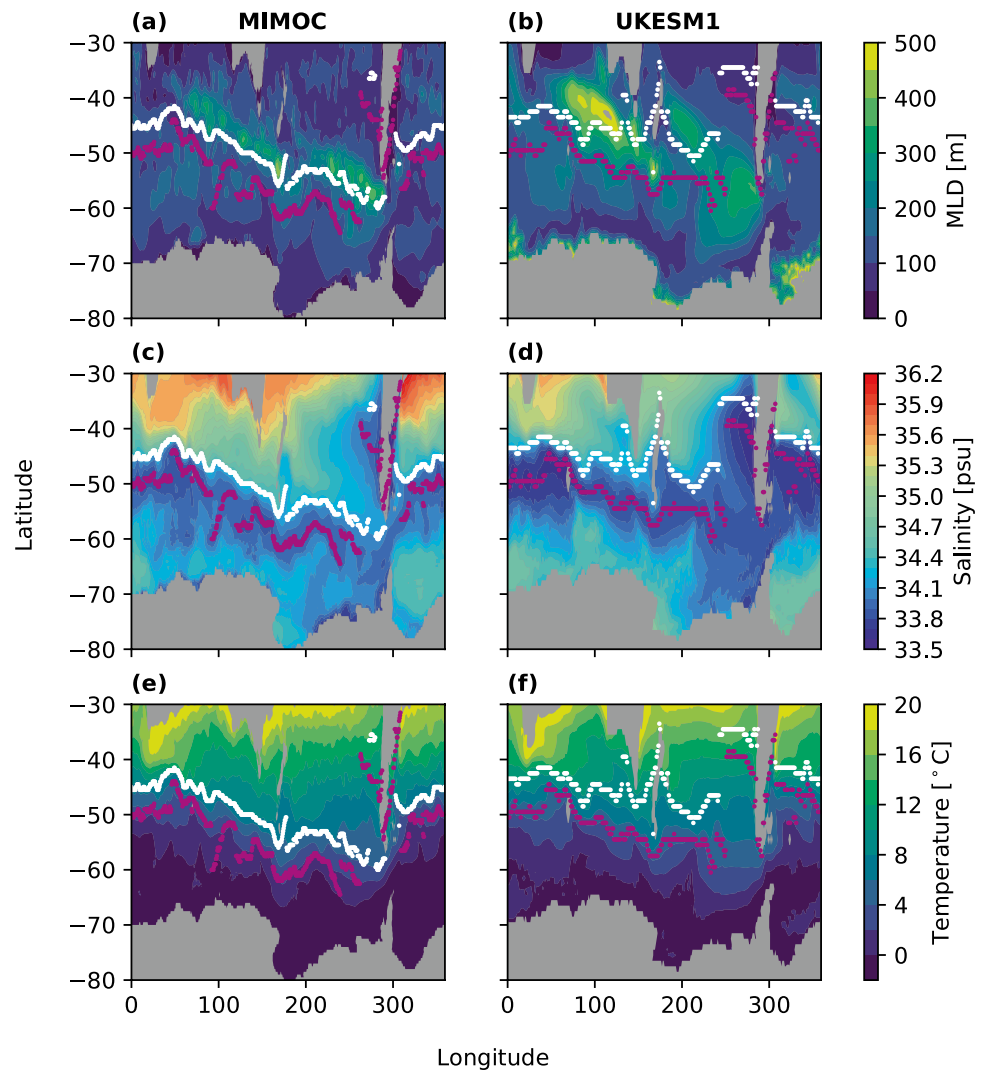
UKESM1 and MIMOC varies between 40° S and 45° S in the Atlantic and Indian oceans which coincides closely to the position of the SAF identified by Treguier et al. (2007) in the ORCA025 (1/4° resolution) configuration of the NEMO model averaged between 1991 and 2000. In the Pacific Ocean, the position matches the one found in Treguier et al. (2007) in MIMOC, but in UKESM1 it is positioned further north (between 45° S and 50° S in the West Pacific and at 35° S in the East Pacific) and does not go through the Drake passage. The differences between MIMOC and UKESM1 will be explored further in Sect. 4. In the following, the location of the southernmost mid-depth salinity minimum is used as an indicator of the location where the core of AAIW is sunk at depth and represents the boundary where stratification ceases to be solely dominated by temperature.

### 3.3 Outcrop of the salinity minimum

South of the southernmost salinity minimum, salinity increases with depth so that the lowest salinity values are found at the surface (Pollard et al. 2002). The region between the southernmost salinity minimum and northernmost temperature minimum corresponds to a region where Turner angles are between  $-45^\circ$  and  $45^\circ$  and therefore does not contain a vertical salinity minimum. The outcrop of the salinity minimum is thus here defined as the position of the meridional salinity minimum at the winter mixed layer depth between 30° S and 60° S. The choice of using the salinity at the winter mixed layer depth instead of at the surface is made to exclude seasonal changes of the mixed layer itself, as it is well known that the interior of the ocean is mostly ventilated in winter at the time of the deepest mixed layer (Williams et al. 1995). The outcrop of the salinity minimum is illustrated as a pink star in Fig. 1b and as a pink line in Fig. 2. The outcrop location shows a similar zonal pattern to the southernmost salinity minimum albeit shifted poleward (Fig. 2).

To summarise, the depth of the salinity minimum and the properties at that depth provide a consistent way to investigate AAIW properties across basins, scenarios and models. The southernmost salinity minimum delimits the region where temperature ceases to dominate stratification over salinity. North of the southernmost salinity minimum, the meridional salinity minimum on the winter mixed layer depth between 30° S and 60° S is used to identify the outcrop of the salinity minimum. The properties of the salinity minimum and its response to a changing climate under different scenario are discussed below.

**Fig. 2** September mixed layer depth (**a** and **b**), surface salinity (**c** and **d**) and surface temperature (**e** and **f**) averaged between 1992 and 2014 for MIMOC and UKESM1 respectively. The location of the southernmost salinity minimum is shown in white and the outcrop location of the salinity minimum in pink



#### 4 UKESM1 model evaluation

This section evaluates the ability of UKESM1 to represent the spatial distribution of AAIW's properties. First, a comparison of the mixed layer depth, surface temperature and salinity between MIMOC and UKESM1 is presented. The properties on the salinity minimum (depth, density, salinity and temperature) are then analysed and compared to MIMOC.

Figure 2 shows the September mixed layer depth (panels a and b), surface salinity (panels c and d) and surface temperature (panels e and f) for MIMOC and UKESM1 respectively. The September mixed layer depth varies between 10 and 505 m in MIMOC and between 2 and 510 m in UKESM1. The deepest mixed layer depths are found between 38° S and 62° S in both MIMOC and UKESM1. The southernmost salinity minimum (in white) is found south of the regions with the deepest mixed layers in both MIMOC and in UKESM1, with the exception of the southeast Pacific in

UKESM1. North of the southernmost salinity minimum, low salinities are found in the southeast Pacific, both in UKESM1 and MIMOC. The surface salinity in the Pacific is fresher in UKESM1 compared to MIMOC. Salinity is low (<34.1 psu) south of the southernmost salinity minimum, in both MIMOC and UKESM1. Surface temperatures in MIMOC and UKESM1 are in good agreement.

Salinity sections together with the density, salinity, temperature and depth of the salinity minimum are shown at longitudes of 90° (Indian), 190° (Western Pacific), 265° (Eastern Pacific) and 335° (Atlantic) for MIMOC and UKESM1 (Fig. 3). The winter mixed layer depth is shown in white. The low salinity tongue spreading from South to North can clearly be identified in both UKESM1 and MIMOC and the salinity minimum is successfully detected in the four sections in UKESM1. For the sections in the Pacific and Indian oceans, the salinity minimum is shallower, warmer, fresher and lighter in UKESM1 compared to MIMOC. In the Indian Ocean, at 30°S the salinity minimum has a depth of 841 m

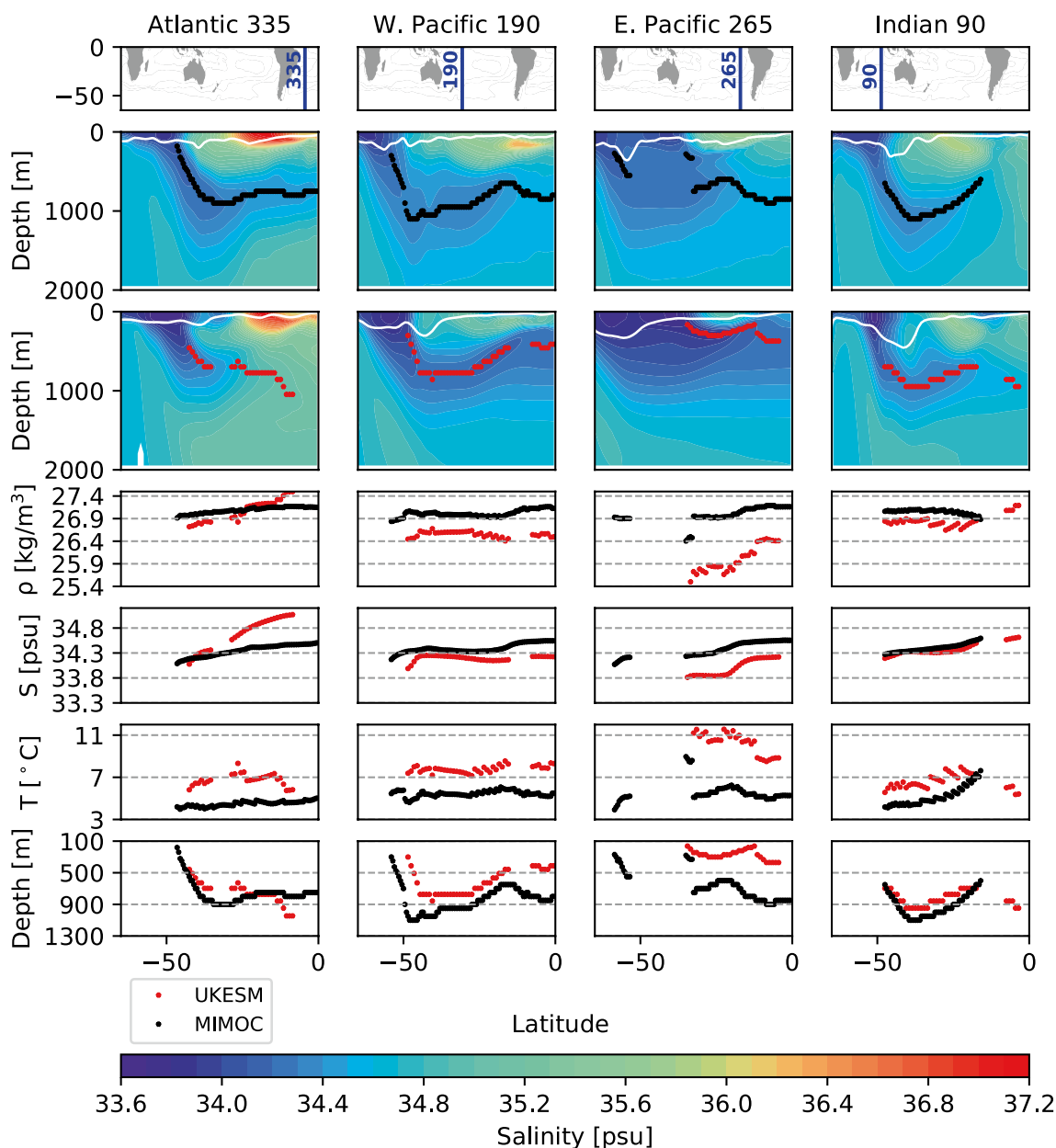


**Fig. 3** Salinity sections for MIMOC (top row) and UKESM1 (second row) with the mixed layer depth shown in white together with the density, salinity, temperature and depth on the salinity minimum for

MIMOC (in black) and the historical run of UKESM1 (in red) in the Atlantic, West Pacific, East Pacific and Indian at longitudes of 335°, 190°, 265° and 90° respectively

(1011 m), temperature of 6.9 °C (5.1 °C), salinity of 34.3 psu (34.3 psu) and density of 26.7 kg/m<sup>3</sup> (27.1 kg/m<sup>3</sup>) in UKESM1 (MIMOC). In the West Pacific, at 30°S the salinity minimum has a depth of 768 m (938 m), temperature of 7.6 °C (5.3 °C), salinity of 34.2 psu (34.3 psu) and density of 26.6 kg/m<sup>3</sup> (27.0 kg/m<sup>3</sup>) in UKESM1 (MIMOC). The differences are larger in the East Pacific where at 30°S the salinity minimum is shallower, warmer, fresher and lighter in UKESM1 (208 m, 11.1 °C, 33.8 psu and 25.8 kg/m<sup>3</sup>)

compared to MIMOC (720 m, 5.2 °C, 34.2 psu and 26.9 kg/m<sup>3</sup>).

Unlike the Indian and Pacific cross sections where the properties appear to be shifted by a bias which remains roughly constant across latitudes, the Atlantic cross section presents varying biases across latitudes. At 42° S, the salinity minimum properties match closely in UKESM1 and MIMOC in terms of depth (545 m in UKESM1 and 569 m in MIMOC) and salinity (34.1 psu in UKESM1 and 34.2 psu in MIMOC) with a lighter salinity minimum in UKESM1

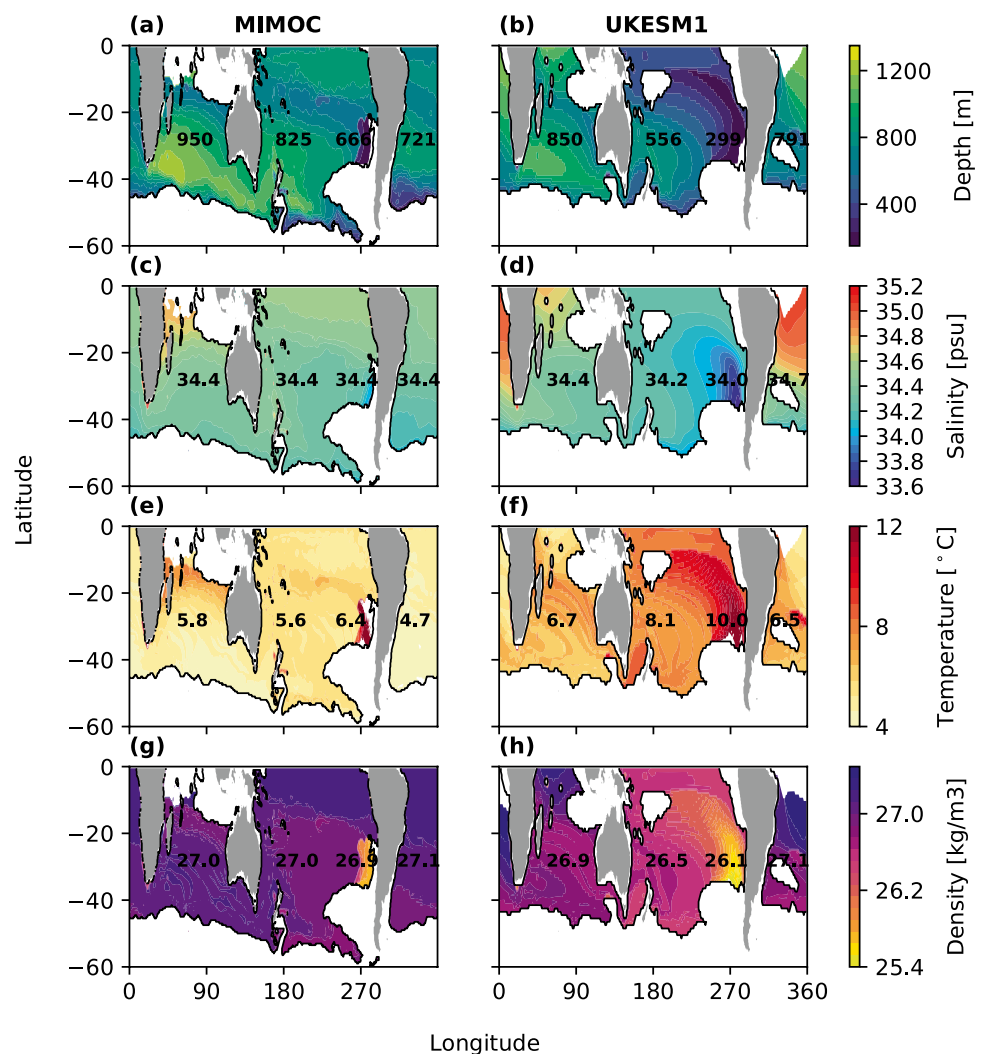
(26.8 kg/m<sup>3</sup> in UKESM1, 27.0 kg/m<sup>3</sup> in MIMOC) and warmer salinity minimum in UKESM1 (5.6 °C in UKESM1, 4.4 °C in MIMOC). As the salinity minimum spreads north, the salinity increases more rapidly in UKESM1 compared to MIMOC with a salinity of 35.1 psu in UKESM1 and 34.5 psu in MIMOC at 10° S. In the Atlantic, the salinity minimum does not extend as far north in UKESM1 compared to MIMOC (8°S in UKESM1 compared to 22°N in MIMOC). The reduced extent of AAIW in the Atlantic basin appears to be a common feature in CMIP5 models (Zhu et al. 2018). Sloyan and Kamenkovich (2007) found that in a study focusing on 8 CMIP3 models, all models presented a reduced northward extent of the salinity minimum in the Atlantic Ocean compared to observations. They suggest the reduced extent is due to models being too diffusive. As AAIW plays a key role in the return northward flow, a reduced extent can have implications in the model's ability to represent the overturning circulation accurately.

Figure 4 shows maps of the depth of the salinity minimum, and the salinity, temperature and density at that

depth for MIMOC and UKESM1. The mean values for the Indian, West Pacific, East Pacific and Atlantic basins are shown in black. On average, the salinity minimum of each basin in UKESM1 is warmer (6.7 °C, 8.1 °C, 10.0 °C and 6.5 °C for the Indian, West Pacific, East Pacific and Atlantic basins respectively) compared to MIMOC (5.8 °C, 5.6 °C, 6.4 °C and 4.6 °C for the Indian, West Pacific, East Pacific and Atlantic basins respectively). The West and East Pacific in UKESM1 have a fresh bias of 0.2psu and 0.4psu and a light bias of 0.5 kg/m<sup>3</sup> and 0.8 kg/m<sup>3</sup> respectively, while the salinity minimum in the Atlantic basin has a salty (0.3 psu) bias. Large zonal differences in properties can be found between the East and West Pacific, where in the southeast a shallow (299 m), light (26.1 kg/m<sup>3</sup>), fresh (34.0 psu) and warm (10 °C) patch can be found. To isolate the anomaly in the East Pacific, we here split the Pacific at 240°.

UKESM1 and MIMOC present some similarities in basin to basin characteristics of the salinity minimum. For example, the deepest salinity minimum is found in the

**Fig. 4** Depth, salinity, temperature and density on the salinity minimum for MIMOC (a–d) and UKESM1 (e–f). The mean values per region are displayed in black (Atlantic, Indian, East and West Pacific). Areas in white correspond to areas where the salinity minimum is not detected





Indian ocean (average of 950 m in MIMOC and 850 m in UKESM1) and the shallowest in the East Pacific (average of 666 m in MIMOC and 299 m in UKESM1). The salinity minimum is also lighter and warmer in the Pacific compared to the Atlantic in both MIMOC and UKESM1. Differences between the Pacific and Atlantic are however greater in UKESM1, with a temperature and density difference of 1.6 °C and 0.6 kg/m<sup>3</sup> between the West Pacific and Atlantic in UKESM1 compared to only 0.9 °C and 0.1 kg/m<sup>3</sup> in MIMOC.

The largest differences in properties between UKESM1 and MIMOC are found in the southeast Pacific. There, the salinity minimum in UKESM1 is too shallow and fresh. In MIMOC, a shallow local salinity minimum can be distinguished above the intermediate salinity minimum detected (black dots, Fig. 2). This shallow local salinity minimum is responsible for the small region with anomalous values in MIMOC found between 32°S and 35° S in the East Pacific section in Fig. 2 and as well as at 270° in Fig. 4. (panels a, e and g) where the salinity minimum is shallower, warmer and lighter than its surrounding value. This local salinity minimum corresponds to East South Pacific Intermediate Water (ESPIW), which forms due to large precipitation and freshwater fluxes off the coast of Chile (Schneider 2003). In UKESM1 however, the ESPIW and AAIW layers are not well separated in salinity and there is only a unique salinity minimum that can be detected in the southeast Pacific region. Since the formation of this feature in UKESM1 is clearly different than in MIMOC, the local salinity minimum in the southeast Pacific is likely not a good diagnostic for AAIW in that localised region, which is somewhat of a paradox since this is the region where much of Pacific-type AAIW is believed to form. Nevertheless, this model bias points to shortcomings of the UKESM1 simulations in the southeast Pacific region. On one hand, this problem illustrates limits of using local vertical extrema for tracing water masses as these depend on relative differences and therefore the local context, but this also shows that biases in extrema detection can be used to identify model biases effectively. The bias in the southeast Pacific could be due to the model being too diffusive which does not allow formation of a shallow local extrema in salinity.

The comparison between UKESM1 and MIMOC shows that overall UKESM1 is able to characterise the salinity minimum feature in all basins, albeit in the East Pacific. Although the salinity minimum has a warm and light bias globally, relative trends capture basin to basin differences.

## 5 Response of the salinity minimum to different radiative forcing scenarios

The ScenarioMIP simulations of UKESM1 provide a way to assess the sensitivity of the salinity minimum to different radiative forcing scenarios. Changes in the salinity minimum properties are here quantified for the 2080–2100 time mean for all the different future scenarios and the corresponding piControl run. The historical run (1992–2014 time mean) from Sect. 4 is added for completeness. The aim of this section is to assess the impact of radiative forcing on the salinity minimum with first a focus on the outcrop location (Sect. 5.1) and then on the properties at depth (Sect. 5.2).

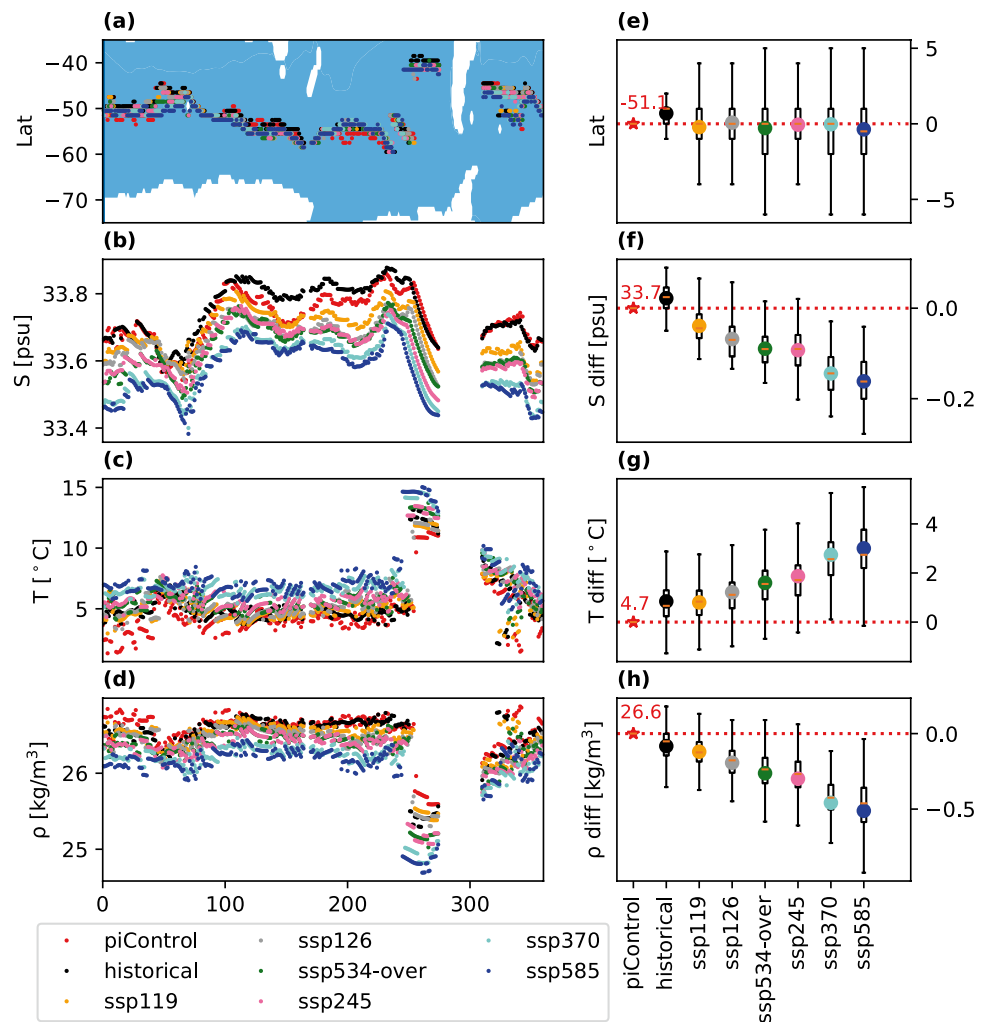
### 5.1 Stability of the outcrop location of the salinity minimum

A striking feature in Fig. 5a, which shows the latitude of the outcrop of the salinity minimum for the different ScenarioMIP simulations, is that the position of the outcrop remains constant in UKESM1, irrespective of changes in radiative forcing. The outcrop of the salinity minimum is located on average at 51° S, with a northernmost position at 40° S in the East Pacific and a southernmost position at 59° S in the West Pacific. In the Atlantic, the latitude of the outcrop varies between 45° S and 55° S. In the Indian, the latitude of the outcrop is located around 50° S and shifts poleward to around 55° S in the West Pacific. The mean anomalies of the latitude, salinity, temperature and density compared to piControl are shown for each simulation in Fig. 5e–h, together with the interquartile range and median. Figure 5e shows that although there is some regional variability, there is no clear shift either south or north with increased radiative forcing. The mean anomalies in latitude vary between 0.5° N and –0.4° S but there is no systematic trend with radiative forcing (i.e. across scenarios).

The salinity, temperature and density at the outcrop of the salinity minimum are shown in Fig. 5b–d. Values between 165° and 175° and between 275° and 310° are not shown in Fig. 5a–d as they represent low salinity waters from the coasts of New Zealand and South America respectively. In contrast to the latitude of the outcrop which remains stable across the different scenarios, the salinity, temperature and density of the outcrop show clear and large shifts as the radiative forcing is increased.

Changes in outcrop properties are consistent across all longitudes, with properties getting fresher, warmer and hence lighter at the outcrop of the salinity minimum as radiative forcing is increased. The salinity at the outcrop shifts

**Fig. 5** Longitudinal variation in **a** latitude, **b** salinity, **c** temperature and **d** density along the outcrop location of the salinity minimum for the piControl, historical and SSP scenarios. Panels **e–h** show the longitudinal mean values (coloured dots) of the anomaly compared to piControl together with a box plot showing the interquartile range. The whiskers of the boxplot are calculated as  $Q3 + 1.5 \cdot (Q3 - Q1)$  and  $Q1 - 1.5 \cdot (Q3 - Q1)$  where  $Q1$  and  $Q3$  are the quartile values of the data



to fresher values as the radiative forcing is increased, with the difference between piControl and the most extreme scenario (SSP5-8.5) equal to 0.16 psu. The temperature at the outcrop gets warmer with increased radiative forcing with a mean temperature change of 3.0 °C between the piControl and the SSP5-8.5 simulations. The density at the outcrop follows the temperature and salinity trends and gets lighter with increased radiative forcing with a mean difference of 0.5 kg/m<sup>3</sup> between the piControl and the SSP5-8.5 simulations. The similarities in longitudinal trends in both temperature and density suggest that density changes are dominated by temperature changes.

## 5.2 Properties at depth on the salinity minimum

Maps of the depth, density, salinity and temperature differences between the piControl run and SSP5-8.5 scenarios are shown in Fig. 6 and provide an indication of the changes induced by the most extreme scenario. Overall, on average over the southern hemisphere, the salinity minimum shoals (−82 m), lightens (−0.3 kg/m<sup>3</sup>), freshens

(−0.08 psu) and warms (+1.7 °C). Although zonal averages present a useful overview of changes globally, they cannot inform on basin to basin variability and intra-basin variability. As more data is obtained in the Southern Ocean, recent studies highlight the existence and importance of zonal structures in both physical and biochemical properties (Noh et al. 2021). Looking at regional averages instead of global averages (with the Pacific basin split into East and West Pacific at 240° as in Sect. 4) shows that the largest response to climate change forcing occurs in the West Pacific with a shoaling of −116 m, a lightening of −0.4 kg/m<sup>3</sup>, a freshening of −0.14 psu and warming of +1.9 °C.

Although basin averages provide a good estimate of changes in the Indian and West Pacific, the changes within the Atlantic and East Pacific are not uniform and present some contrasting anomalies. For instance, the West Pacific presents the largest basin-averaged change. In absolute term, the most sensitive area is the southeast Pacific. However, as discussed above, the vertical salinity gradient in the southeast Pacific in UKESM1 is not adequately resolved. It is

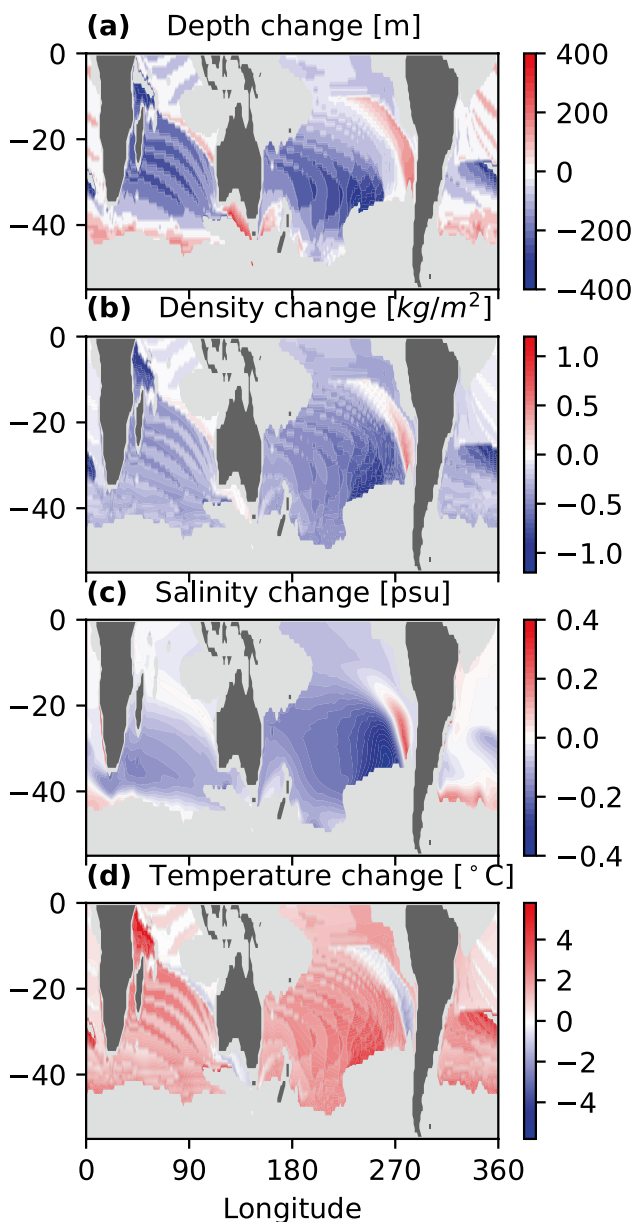


**Fig. 6** Depth, density, salinity and temperature difference (a–d respectively) on the salinity minimum between the SSP5-8.5 and piControl run

not clear what impact this bias has on the properties of the salinity minimum overall or how systematic this bias is in CMIP-class models. The salinity minimum in the Atlantic overall gets warmer (+1.6 °C) and lighter ( $-0.24 \text{ kg/m}^3$ ).

Figure 7 shows the depth, density, salinity and temperature for all scenarios in four sections at 90° (Indian), 190° (West Pacific), 265° (East Pacific) and 335° (Atlantic). The aim here is to assess how the different scenarios impact the properties on the salinity minimum as well as to analyse further the basin-to-basin differences. The ScenarioMIP simulations overall show similar trends to the SSP5-8.5 scenario

with smaller magnitudes. In the Atlantic, salinity remains constant in all scenarios, with a latitudinal increase of 1 psu between 45° S and 10° S in all scenarios. The East Pacific shows a sharp zonal variation at 20° S, with properties north of 20° S showing a steep increase in density, salinity and temperature. In the Atlantic, the changes are not constant with latitude, with the largest differences in density, depth and temperature at 30° S.

Although changes in depth, density, salinity and temperature are projected, the meridional extent of the salinity minimum appears to remain unchanged in all scenarios. In addition, in the Atlantic, the salinity at the depth of the salinity minimum does not change in the different scenarios. The next section explores the mechanisms which lead to the relative stability of the outcrop of the salinity minimum while other hydrographic properties all seem to respond to changing radiative forcing.

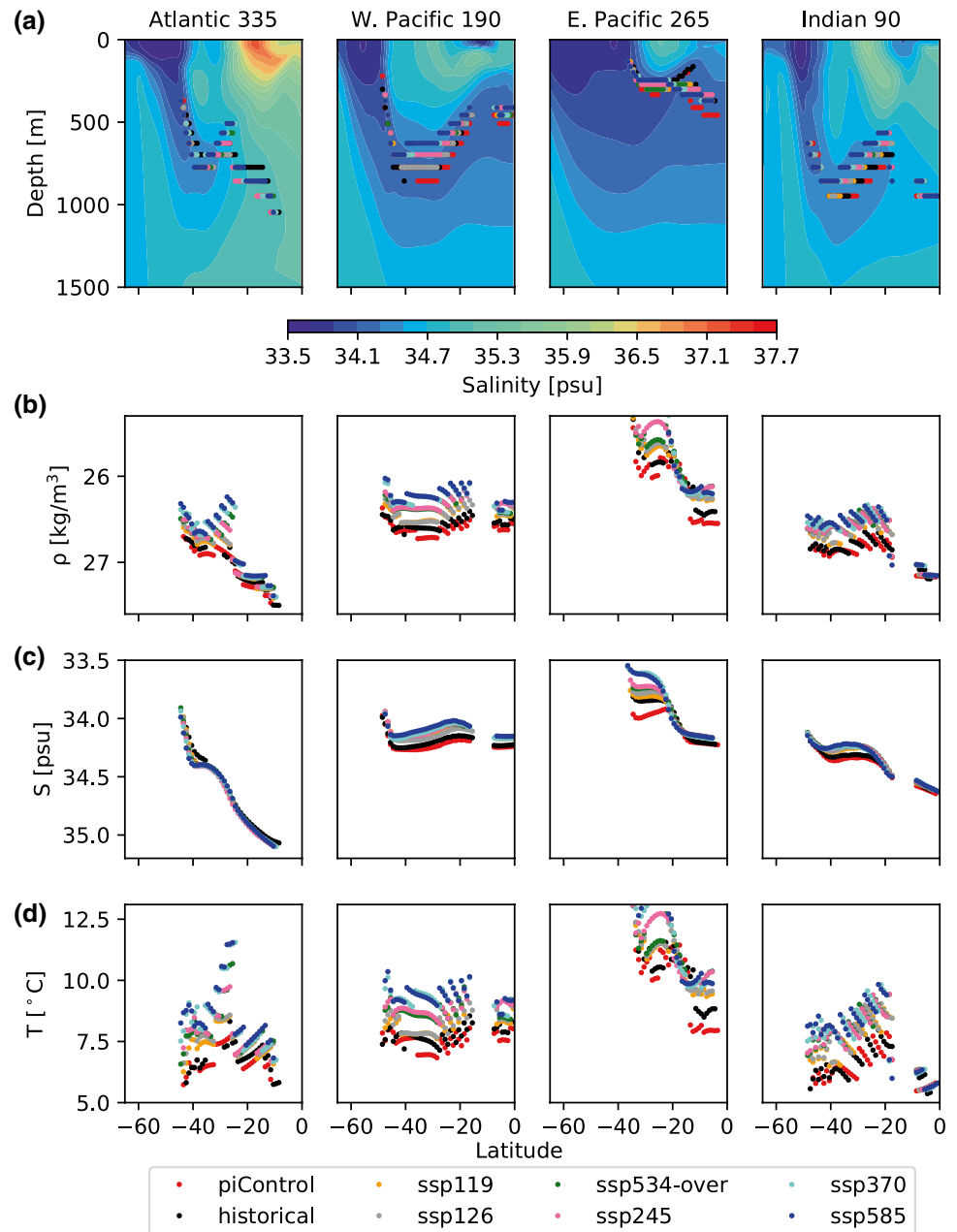
## 6 Stability driving mechanisms in the Southern Ocean

Although the position of the outcrop of the salinity minimum is stable, the salinity, temperature and density at the outcrop of the salinity minimum all respond to changes in radiative forcing. The question is then why the outcrop location can remain stable when hydrographic properties are all responding to climate forcing. In particular, one may question whether the stability is specific to the salinity minimum feature or whether it is linked to an overall stability of frontal locations in the Southern Ocean. To shed light on the origins of the stability, the possible change of the position of the ACC under radiative forcing is investigated. The role of wind stress and topography in modulating the stability of the ACC is assessed (Sect. 6.1). In addition, the air-sea fluxes are analysed to link atmospheric forcing to the changes observed on the salinity minimum (Sect. 6.2).

### 6.1 Fronts and ACC structure

To analyse the stability of fronts within the ACC, the position of the maximum gradient in sea surface height and the barotropic streamfunction are calculated. The maximum gradient in the sea surface height field is used to estimate how the ACC changes position in response to changes in radiative forcing (Graham et al. 2012). Although studies have shown that ACC fronts are composed of multiple filaments (Chapman et al. 2020), the coarse resolution (1 degree) of the model and temporal averaging does not allow for an accurate representation of these filaments. Figure 8 shows the location of the maximum gradient in sea surface height for the different scenarios together with the piControl sea surface height gradient field. The positions of the maximum

**Fig. 7** **a** piControl salinity section (background) together with the depth of the salinity minimum detected for each scenario (coloured points). Other panels show the **b** density **c** salinity **d** temperature at the salinity minimum for each scenario (coloured dots) along the Atlantic, West Pacific, East Pacific and Indian Oceans sections



gradient in sea surface height present some local differences around the Drake passage but overall appear to remain at the same location irrespective of radiative forcing (Fig. 8). The stability of the position of the sea surface height maximum gradient suggests that the ACC core does not vary in location with increasing radiative forcing.

The barotropic streamfunction is shown in Fig. 9 for the piControl and SSP5-8.5 runs. The southernmost and northernmost contours going through Drake passage provide an indication of the ACC pathway and are shown in green in Fig. 9. The positions of the maximum gradient in sea surface height and the salinity minimum outcrop are shown in blue and red respectively. The positions of the

maximum sea surface height gradient and salinity minimum outcrop match in the East Indian and Atlantic but differ in the East Pacific. The outcrop of the salinity minimum is located between the southernmost and northernmost barotropic streamfunction contours that bound Drake passage, which strengthens the idea that the stability of the outcrop of the salinity minimum is linked to an overall stability of the ACC in the UKESM1 simulations. The stability results agree with results from Graham et al. (2012) who showed that frontal locations within the ACC do not shift poleward in the higher resolution ( $1/3^{\circ} \times 1/3^{\circ}$ ) coupled climate model HiGEM either when comparing the final 30 years of the control simulation (335 ppm  $\text{CO}_2$  concentrations) and climate

**Fig. 8** piControl meridional gradient field of sea surface height (SSH) (background) together with the position of the maximum meridional SSH gradient for each scenario (coloured dots, model legend as in Fig. 7)

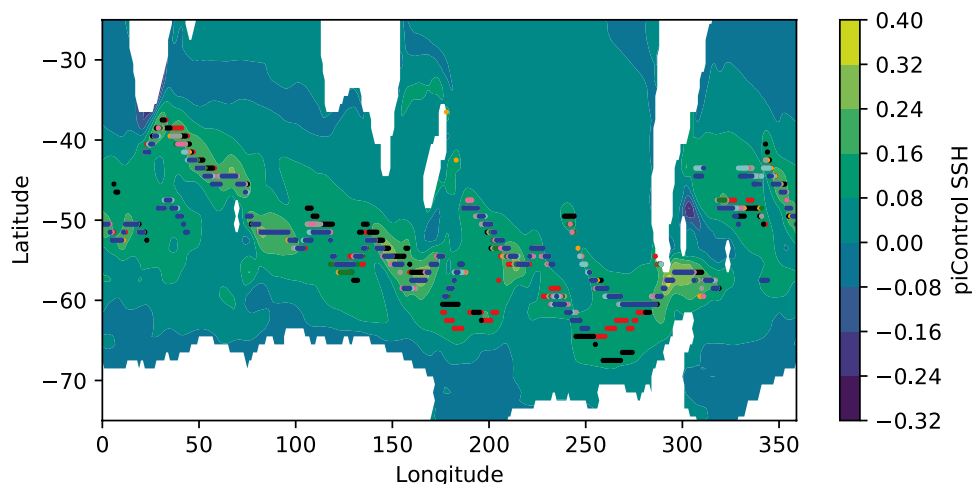
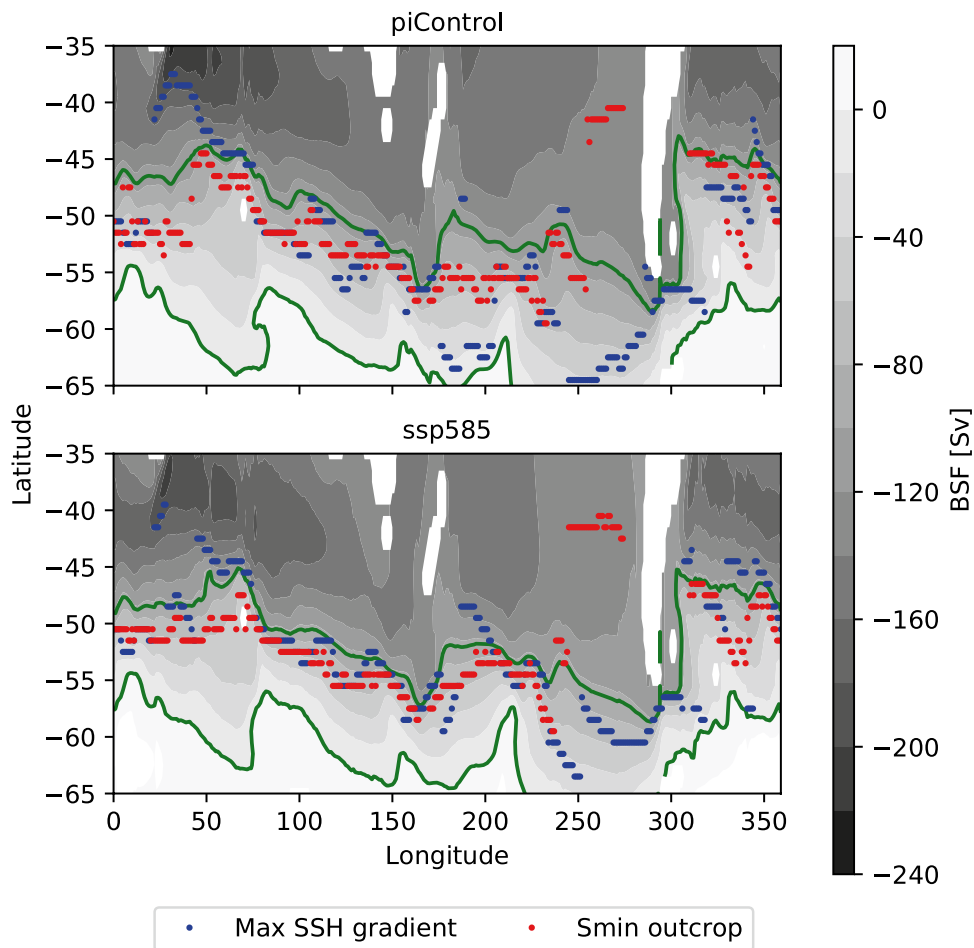


**Fig. 9** Contour plot of the barotropic streamfunction (BSF) for the piControl (top) and SSP5-85 scenario (bottom) showing also the contours (green lines) of the northernmost and southernmost value of BSF identified across the Drake passage. The position of the maximum sea surface height (SSH) gradient and of the salinity minimum (Smin) outcrop for the piControl and SSP5-8.5 simulations are shown with blue and red dots, respectively

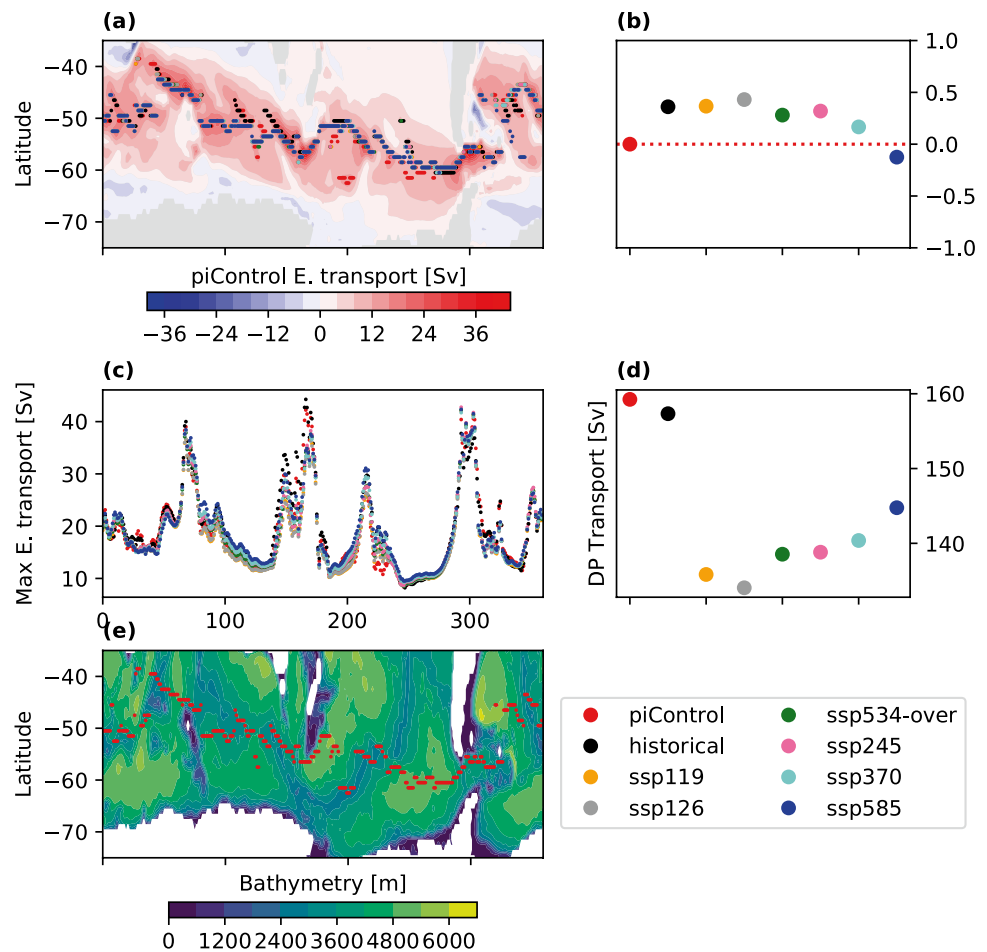


change simulation (2% increase of CO<sub>2</sub> concentrations for 70 years until concentrations reach 4× control simulation CO<sub>2</sub> concentrations).

To provide a quantitative measure of the transport within the ACC, the eastward transport (calculated as the depth integrated eastward flow) is analysed. Figure 10a shows the piControl eastward transport (background) and

the location of the maximum eastward transport for the different scenarios (coloured dots). Figure 10b shows the mean difference (coloured dots) for the different simulations compared to the piControl run for the position of the maximum eastward transport. The position of the maximum eastward transport varies between 61° S at the Drake passage and 40° S in the Indian Ocean. Similarly

**Fig. 10** **a** Depth-integrated eastward transport for the piControl simulation together with the location of the maximum depth-integrated eastward transport for each scenario (coloured dots). **b** Zonally averaged difference in meridional position of the depth integrated eastward transport calculated as the difference between the various scenarios and the piControl simulation (positive values show a northward shift relative to the piControl case). **c** Longitudinal variation of the maximum depth integrated eastward transport. **d** Transport through Drake passage at  $296^\circ$ . **e** Topography of the Southern Ocean in the UKESM1 model



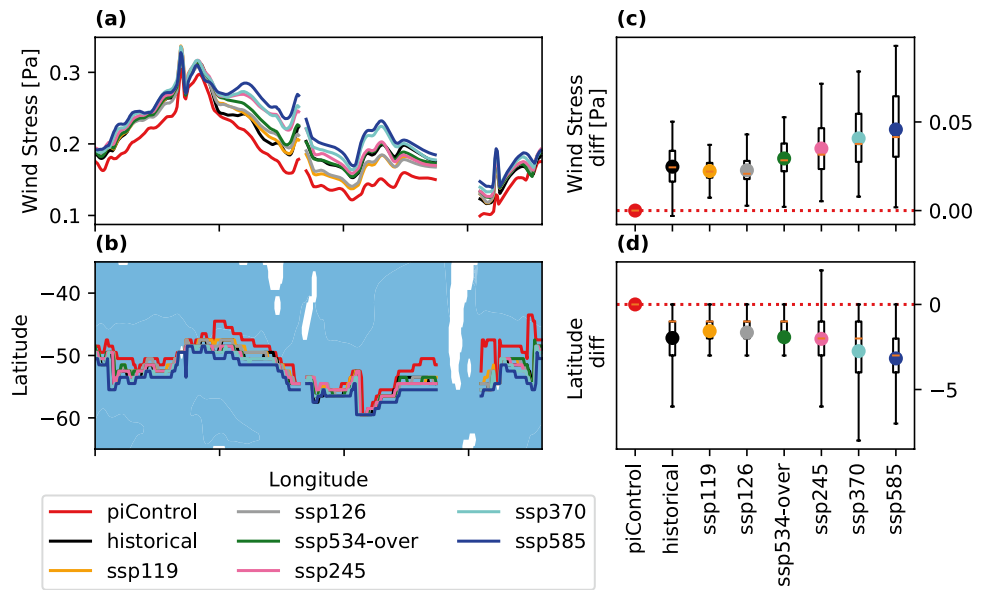
to the salinity minimum outcrop and the maximum sea surface height gradient, the position remains stable in all scenarios, with the mean change in latitude between each scenario relative to the piControl scenario remaining smaller than  $0.6^\circ$  (Fig. 10b). The transport through Drake passage is calculated as the sum of the eastward transport at  $296^\circ$  and is shown in Fig. 10d. Values vary between 134 Sv (SSP1-2.6 scenario) and 159 Sv (piControl simulation). There is no clear link between either the maximum eastward transport values or transport through Drake passage and radiative forcing. The transport at Drake passage from the historical simulation is equal to 157 Sv and is slightly lower than in observations: Donohue et al. (2016) calculated a transport of 173 Sv based on measurements from 2007 to 2011.

Two main drivers are commonly assessed when analysing changes in position of the ACC: bottom topography and wind stress (Graham et al. 2012). The bottom topography of the model is shown in Fig. 10e together with the location of the maximum eastward transport (in red) for the piControl run. The magnitude of the maximum eastward transport is plotted in Fig. 10c. The locations of the peaks in Fig. 10c correspond to areas where the ACC is constrained by bottom

topography (Fig. 10e): through Drake passage, the ACC is constrained both north and south by South America and Antarctica. The peak at  $167^\circ$  is constrained north by the Campbell Plateau and the peak at  $68^\circ$  S by the Kerguelen Plateau. It should be noted that the magnitude of the peaks should be assessed cautiously as the transport in the model may be saturated as a result of the eddy parameterisation used. Intermodel comparisons will help assess the influence of such parameterisations in controlling the apparent stability of the salinity minimum outcrop.

The maximum meridional wind stress has been shown to play a key role in driving the ACC (Lin et al. 2018) and its position and magnitude are here analysed. The position and magnitude of the maximum meridional wind stress for the different scenarios are shown in Fig. 11a, b. The location of the maximum meridional wind stress shifts poleward as radiative forcing increases. The mean change between the position for the SSP5-8.5 and for the piControl run is equal to  $3.2^\circ$  in latitude. The mean maximum meridional wind stress also gets stronger as radiative forcing increases (Fig. 11c), with a mean difference of 0.05 Pa between the piControl (0.18 Pa) and SSP5-8.5 scenarios (Fig. 11d). The poleward shift and intensification of the wind stress under a

**Fig. 11** Longitudinal variation of **a** the maximum meridional wind stress, **b** the latitude of the maximum meridional wind stress for the piControl, historical and SSP scenarios respectively. Differences in zonally-averaged **c** maximum wind stress magnitude and **d** latitudinal position of the maximum wind stress point between the various scenarios and piControl simulation (coloured dots). Box and whiskers plot showing the interquartile range (**d–f**). The whiskers are calculated as  $Q3 + 1.5*(Q3-Q1)$  and  $Q1 - 1.5*(Q3-Q1)$  where  $Q1$  and  $Q3$  are the quartile values of the data



warming climate in the Southern Ocean has been observed in the results from previous studies based on CMIP5 simulations (Bracegirdle et al. 2013; Meijers 2014). The results are consistent with the idea that it is bottom topography rather than wind stress that controls the position of the core of the ACC in the UKESM1 model, in agreement with Graham et al. (2012) in the higher resolution HIGEM. This is also consistent with the results of Meijers (2012) who found that there is no correlation in CMIP5 models between the westerly wind jet and the ACC position in future scenarios in a study where 23 CMIP5 models are assessed and with the results of Beadling et al. (2019) who show that the position and strength of the westerly winds are not correlated with the ACC strength in CMIP5 models. If bottom topography is indeed the main control on the position and structure of the ACC, then bottom topography could likely also control the stability of the outcrop location of the salinity minimum outcrop.

**6.2 Air–sea fluxes**

While the constant position of the salinity minimum outcrop can be linked to an overall stability of the ACC structure, changes in properties are observed both at the surface (Sect. 5.1) and at depth (Sect. 5.2). The air–sea fluxes are

here assessed to link the changes in buoyancy at the surface to changes in the ocean interior by evaluating the density fluxes and transformation rates in the Southern Ocean.

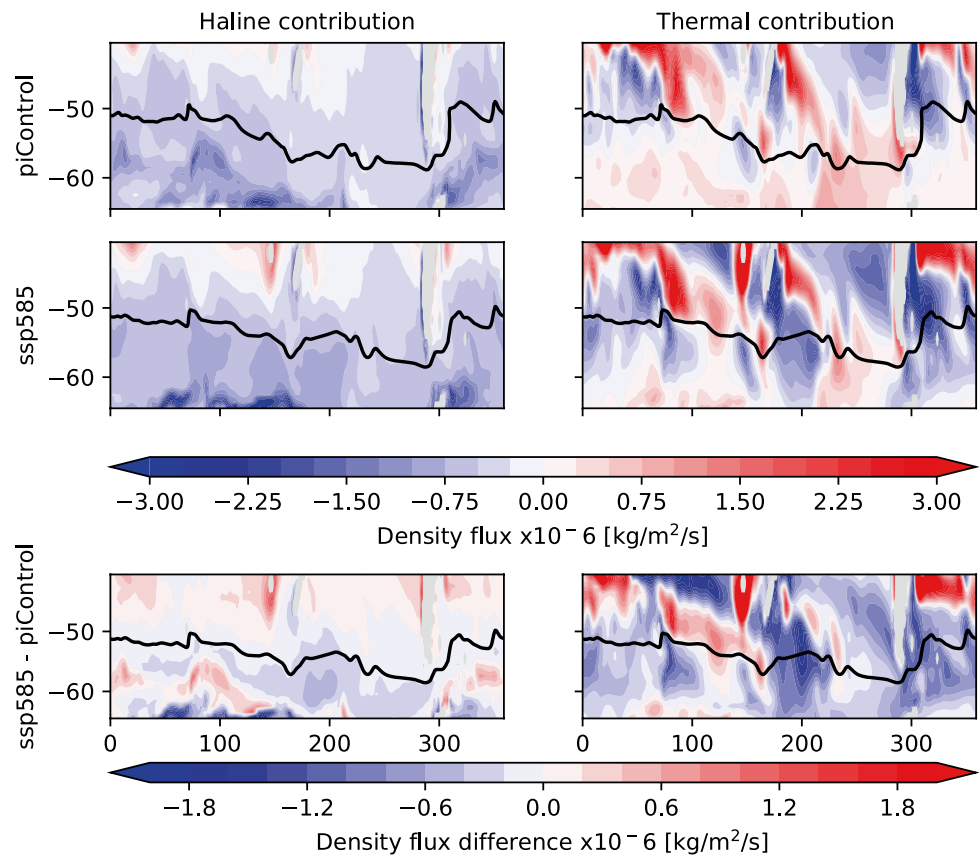
The changes in surface density are here investigated to evaluate the relationship between the air–sea fluxes and the properties at the salinity minimum. The density layer at the salinity minimum ( $\rho_{smin}$ ) is defined as the zonal mean density at the outcrop of the salinity minimum as plotted in Fig. 5h. The density corresponding to the salinity minimum,  $\rho_{smin}$ , together with the shift in density between each simulation and the piControl run ( $\Delta\rho_{smin}$ ) are given in Table 1.

The haline and thermal contributions to the density flux are shown in Fig. 12 for the piControl and SSP5–8.5 simulations. The black line shows the contour corresponding to  $\rho_{smin}$  from Table 1. The haline contribution shows consistently negative values along the density contour in both simulations (between  $-0.25 \times 10^{-6}$  kg/m<sup>2</sup>/s and  $-1.5 \times 10^{-6}$  kg/m<sup>2</sup>/s) indicating that the haline component of the density flux contributes to a lightening of the surface densities. The thermal contribution along the  $\rho_{smin}$  contour presents both negative and positive values, with negative values in the Atlantic and part of the Indian oceans (between  $-0.25 \times 10^{-6}$  kg/m<sup>2</sup>/s and  $-2.0 \times 10^{-6}$  kg/m<sup>2</sup>/s) but positive values in the East Pacific (between  $0.25 \times 10^{-6}$  kg/m<sup>2</sup>/s and  $1.0 \times 10^{-6}$  kg/m<sup>2</sup>/s). The difference

**Table 1** Mean density at the outcrop of the salinity minimum  $\rho_{smin}$  for each simulation along with the density difference  $\Delta\rho_{smin}$  between the piControl simulation and the different scenarios

Scenario	piControl	Historical	SSP1-1.9	SSP1-2.6	SSP5-3.4-over	SSP2-4.5	SSP3-7.0	SSP5-8.5
Mean $\rho_{smin}$ [kg/m <sup>3</sup> ]	26.55	26.47	26.43	26.36	26.29	26.25	26.09	26.04
$\Delta\rho_{smin}$ [kg/m <sup>3</sup> ]	0	0.08	0.12	0.19	0.26	0.30	0.46	0.51

**Fig. 12** Maps of the haline ( $-\beta SF_{wf}$ ) and thermal ( $-\alpha H_{net}/C_p$ ) contributions to the density flux for the piControl and SSP5-8.5 scenarios (top two rows) together with the differences in haline and thermal density fluxes between SSP5-8.5 and piControl (in  $\text{kg}/\text{m}^2/\text{s}$ ) (bottom row). The contour of the density corresponding to the salinity minimum  $\rho_{\text{smi}}$  is shown in black



between the SSP5-8.5 and piControl simulations shows that, overall, the changes in surface density fluxes lead to a lightening of the surface density. The difference is larger in the thermal contributions than in the haline contributions where the difference is closer to zero.

The density flux integrated over density outcrop areas and time provides the transformation rates (Sect. 2.3). Figure 13 shows the transformation rates, together with the corresponding thermal and haline contributions and the formation rates split into basins for the different scenarios. As the aim is to compare the differences in transformation and formation rates corresponding to the salinity minimum, the curves are shifted by  $\Delta\rho_{\text{smi}}$  to be aligned at the density  $\rho_{\text{smi}}$  as defined in Table 1.

The focus is first set on the global average of transformation and formation rates. The  $\rho_{\text{smi}}$  density contour is located in a region of decreasing transformation rates with negative gradients (between  $-27$  Sv and  $-31$  Sv) corresponding to positive formation rates (between 2 and 5 Sv). There is no clear pattern between the radiative forcing and the transformation and formation magnitudes at  $\rho_{\text{smi}}$ . The negative transformation values at  $\rho_{\text{smi}}$  indicate a lightening of the surface waters. The peak formation rates at  $26.2 \text{ kg}/\text{m}^3$  for the piControl simulation corresponds to lighter mode waters. All scenarios maintain similar trends to the piControl scenario with the main change observed being a flattening

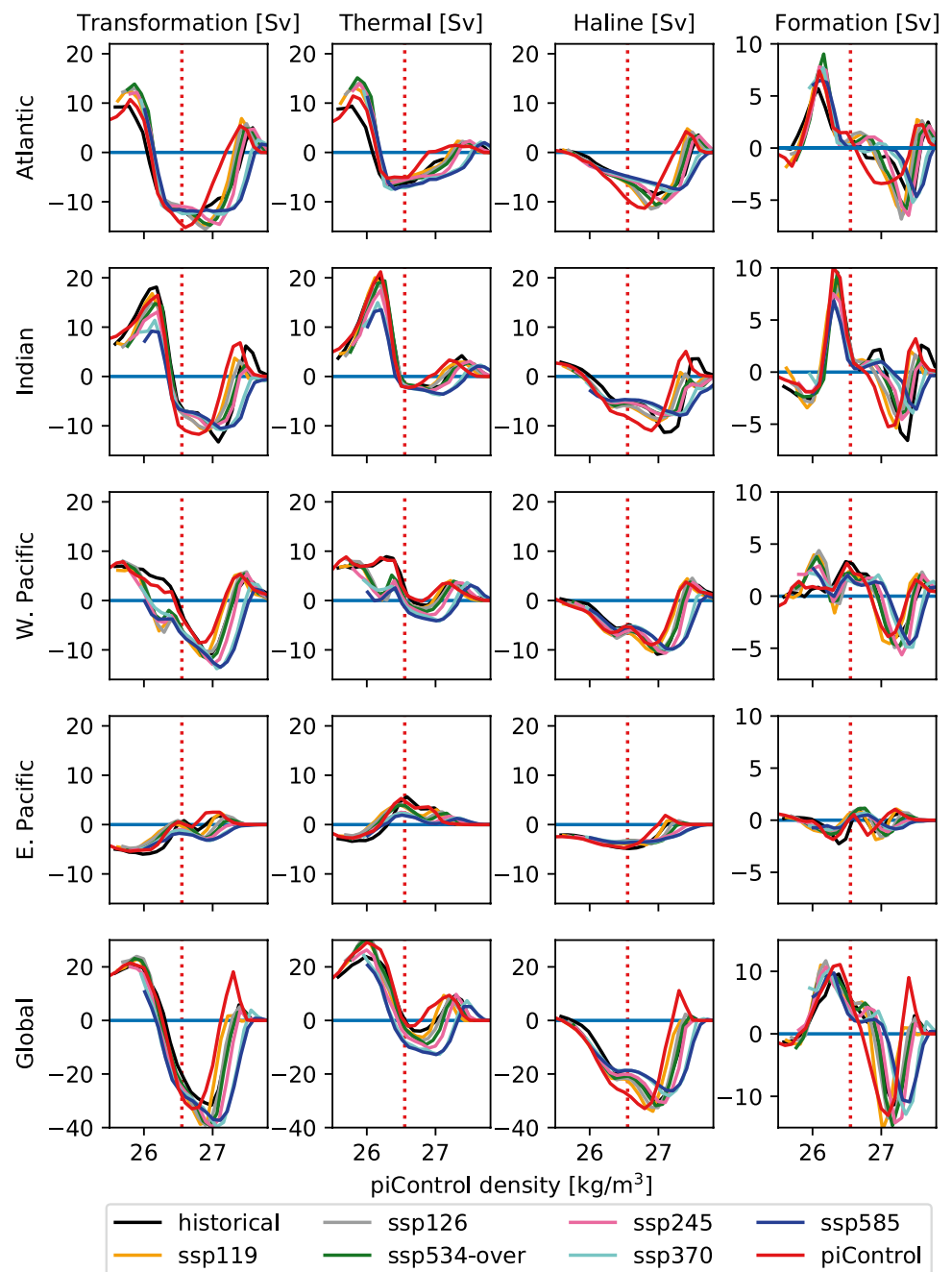
of the transformation and formation curves around  $\rho_{\text{smi}}$  as radiative forcing is increased. The overall shape of the global transformation rate is in agreement with Williams and Follows (2011) where the transformation rates are calculated in the Southern Ocean using the National Oceanography Centre (NOC) surface heat and freshwater fluxes.

The global haline and thermal contributions to the transformation rate present a clear shift, but the haline and thermal shifts compensate one another's effect on density, with higher haline contributions at  $\rho_{\text{smi}}$  for higher radiative forcing scenarios (from  $-29$  Sv for the piControl run to  $-19$  Sv for the SSP5-8.5 scenario) and lower thermal contributions at  $\rho_{\text{smi}}$  for higher radiative forcing scenarios (from  $-2$  Sv for the piControl run to  $-11$  Sv for the SSP5-8.5 scenario). Although the haline contribution to the density flux appears to decrease with higher radiative forcing at  $\rho_{\text{smi}}$  (Fig. 12), the outcrop area also decreases at  $\rho_{\text{smi}}$  (Fig. 14) and as a result the haline contribution to transformation increases. For the thermal contribution to the transformation rate, the decrease of the thermal contribution to the density flux is larger and therefore is not completely counteracted by the decrease in area. The decrease in haline and thermal contributions to the density flux could be linked to an increase in precipitation and temperature.

To explore the basin-to-basin variability, the transformation and formation rates (including haline and thermal



**Fig. 13** Transformation rates, thermal and haline contributions to the transformation rates and the formation rates for the Atlantic, Indian, West Pacific, East Pacific and Global regions (rows) for the historical, piControl and SSP scenarios. For each scenario, the density scale was shifted by  $\Delta\rho_{smin}$  (see Table 1), where  $\Delta\rho_{smin}$  is the difference in the density corresponding to the salinity minimum ( $\rho_{smin}$ ) between each scenario and the piControl run (Table 1). This shift was applied to centre the analysis on the salinity minimum layer and emphasise relative changes around that layer. The red vertical dashed line corresponds to the piControl  $\rho_{smin}$



contributions) are calculated per region (Atlantic, Indian, East Pacific, West Pacific) and shown in Fig. 13 for the different scenarios. The Atlantic, Indian and West Pacific regions present similar transformation contributions to the global transformation curve, with  $\rho_{smin}$  located in between the maximum and minimum transformation rates. However, transformation in the East Pacific differs from the global transformation curve and does not present a clear maximum value at densities lower than  $\rho_{smin}$ . The formation rates at  $\rho_{smin}$  are overall quite low although they are

slightly higher in the West Pacific (between 1 and 2 Sv compared to between 0 and 1 Sv in the other basins). Under radiative forcing, the thermal contribution decreases in the East (5 Sv for the piControl run compared to 1 Sv for the SSP5-8.5 scenario) and West Pacific (1 Sv for the piControl run compared to -3 Sv for the SSP5-8.5 scenario) but shows little variation in the Atlantic and Indian oceans. On the other hand, at  $\rho_{smin}$ , the haline contribution increases under radiative forcing in the Atlantic (-10 Sv and -5 Sv for the piControl run compared to -5 Sv for

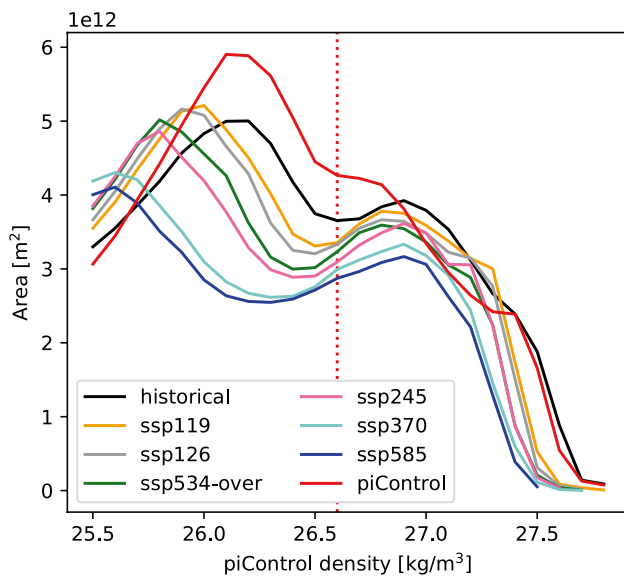


**Fig. 14** Outcrop area for each density interval for different scenarios. For each scenario, the density scale was shifted by  $\Delta\rho_{smin}$  (see Table 1), where  $\Delta\rho_{smin}$  is the difference in the density corresponding to the salinity minimum ( $\rho_{smin}$ ) between each scenario and the piControl run (Table 1). This shift was applied to centre the analysis on the salinity minimum layer and emphasise relative changes around that layer. The red vertical dashed line corresponds to the piControl  $\rho_{smin}$

the SSP5-8.5 scenario) and Indian oceans, while values remain constant in the East and West Pacific.

The density fluxes overall agree with the changes observed on the salinity minimum at depth in Sect. 5 with the decrease in haline and thermal contributions leading to a freshening and warming of the properties at depth under radiative forcing. The density flux itself decreases under radiative forcing which coincides with the lightening of the salinity minimum observed in Sect. 5. On the other hand, the global transformation and formation rates at  $\rho_{smin}$  remain nearly constant irrespective of the radiative forcing due to the counteracting effects of the thermal and haline contributions also due to changes in density outcrop areas.

## 7 Conclusions

The aim of the study was to identify how AAIW, the key water mass in the return flow of fresh water to the Northern Hemisphere, is represented in the UKESM1 CMIP6 model and how its properties evolve under future climate change. The definition of AAIW presented in the study (mid-depth salinity minimum bound by winter mixed layer depth as an upper limit and a depth of 2000 m as the lower limit) provides a consistent way of analysing properties of AAIW across different simulations. Comparing properties on the salinity minimum between UKESM1 and the MIMOC

climatology show that there is, on a global average, a light, shallow, warm and fresh bias in UKESM1 which was also found in other studies focused on CMIP5 and CMIP6 models (Sallée et al. 2013a, b; Beadling et al. 2020).

Future scenarios from the ScenarioMIP simulations show that the outcrop location of the salinity minimum remains stable irrespective of radiative forcing. In contrast, the properties at the location of the outcrop lighten, warm and freshen. Properties at depth also show a lightening and warming of properties across all basins. AAIW evolves differently in the Atlantic compared to the Pacific and Indian basins and shows limited variation in depth and salinity on the salinity minimum. These results show that, while AAIW can be found in the whole Southern Hemisphere, different flavours of AAIW exist in different basins in both MIMOC and UKESM1, and these differ in their response to climate forcing, highlighting the importance of regional phenomena.

The stability of the salinity minimum outcrop coincides with the overall stability of the position of the ACC core. The ACC core appears to be constrained by bottom topography rather than responding directly to changes in the maximum meridional wind stress, which shifts poleward and intensifies. Under radiative forcing, the transformation and formation rates show little variation at the location of the salinity minimum outcrop. While air-sea fluxes do respond to climate forcing, the haline and thermal contributions to transformation tend to counteract one another around the position of the salinity minimum outcrops. In summary, while the salinity minimum changes properties, its formation rate and outcrop location do not change in the different climate scenarios analysed.

Although the results focused on the Southern Ocean, the implications are global as AAIW plays a key role in the freshwater and carbon transport to the Northern Hemisphere. On the one hand, the stability of the outcrop of the salinity minimum, along with the limited changes in formation rates of the core of AAIW and the presence of the salinity minimum in all basins under radiative forcing indicate that the return flow northward and structure of AAIW is overall maintained. In the Atlantic, the depth and salinity appear unaltered under radiative forcing, which could suggest a stability of the boundary between the upper and lower limb of the Atlantic Meridional Circulation. On the other hand, the properties of AAIW overall become warmer and lighter in all basins and fresher in the Pacific and Indian basins under radiative forcing. Given that colder water can store  $\text{CO}_2$  emissions more effectively than warmer water, the increase in temperature observed on the salinity minimum will lead to a reduced carbon storage by AAIW. The carbon storage by AAIW could be further affected by the shoaling of the salinity minimum, which can be accompanied by changes in thickness of AAIW. The increase in temperature along with the freshening of AAIW due to an increase in surface

precipitation leads to a lightening and shoaling of AAIW in the Indian and Pacific basins. The consequences of the shoaling of AAIW in the Indo-Pacific on the overturing circulation are unclear and will require further investigation.

Understanding whether the stability of the outcrop of the salinity minimum is a feature specific to UKESM1 or is systematic across climate models will need to be evaluated. Meijers et al. (2012) did highlight key differences between the CMIP3 and CMIP5 behaviours: unlike CMIP3 models, CMIP5 show no link between the positions of the ACC and westerly winds. Although Beadling et al. (2020) give an overview of the performance of CMIP6 compared to CMIP3 and CMIP5, the stability of the outcrop of the salinity minimum in CMIP6 models remains to be analysed. Importantly, eddies in UKESM1 are parametrised. Analysis of eddy resolving simulations will also be necessary to test the robustness of the stability of the salinity minimum observed here. For instance, Langlais et al. (2015) compared results using both eddy-resolving and eddy-permitting ocean general circulation models to investigate the impact of wind forcing on the ACC. That study highlighted the importance of zonal variation in properties and processes within the Southern Ocean and the continuous need to explore regional differences. Important regional differences are found here as well, indicating that both zonal and meridional differences will need to be considered to better constrain the properties and sensitivity of AAIW in models.

**Funding** This work was supported by the Grantham Institute and the UK NERC Science and Solution of a Changing Planet Doctoral Training Programme at Imperial College London.

**Data availability** The UKESM1-0-LL (Tang et al. 2019) data was obtained through ESGF/CEDA portal (<https://esgf-index1.ceda.ac.uk/projects/esgf-ceda/>). MIMOC (Schmidtko, Johnson, and Lyman, n.d.) data was downloaded from the National Oceanic and Atmospheric Administration (NOAA) portal (<https://www.pmel.noaa.gov/mimoc/>). Data was processed using CDO tools (Schulzweida 2019) and python libraries.

## Declarations

**Conflict of interest** The authors have no relevant financial or non-financial interests to disclose.

**Open Access** This article is licensed under a Creative Commons Attribution 4.0 International License, which permits use, sharing, adaptation, distribution and reproduction in any medium or format, as long as you give appropriate credit to the original author(s) and the source, provide a link to the Creative Commons licence, and indicate if changes were made. The images or other third party material in this article are included in the article's Creative Commons licence, unless indicated otherwise in a credit line to the material. If material is not included in the article's Creative Commons licence and your intended use is not permitted by statutory regulation or exceeds the permitted use, you will

need to obtain permission directly from the copyright holder. To view a copy of this licence, visit <http://creativecommons.org/licenses/by/4.0/>.

## References

- Beadling RL, Russell JL, Stouffer RJ, Goodman PJ, Mazloff M (2019) Assessing the quality of southern Ocean circulation in CMIP5 AOGCM and earth system model simulations. *J Clim* 32(18):5915–5940. <https://doi.org/10.1175/JCLI-D-19-0263.1>
- Beadling RL, Russell JL, Stouffer RJ, Mazloff M, Talley LD, Goodman PJ, Sallée JB, Hewitt HT, Hyder P, Pandde A (2020) Representation of southern Ocean properties across coupled model intercomparison project generations: CMIP3–CMIP6. *J Clim* 33(15):6555–6581. <https://doi.org/10.1175/JCLI-D-19-0970.1>
- Bracegirdle TJ, Shuckburgh E, Sallee J-B, Wang Z, Meijers AJS, Bruneau N, Phillips T, Wilcox LJ (2013) Assessment of surface winds over the Atlantic, Indian, and Pacific Ocean Sectors of the Southern Ocean in CMIP5 Models: historical bias, forcing response, and state dependence. *J Geophys Res Atmos* 118(2):547–562. <https://doi.org/10.1002/jgrd.50153>
- Carmack EC (2007) The alpha/beta ocean distinction: a perspective on freshwater fluxes, convection, nutrients and productivity in high-latitude seas. *Deep-Sea Res Part II Top Stud Oceanogr* 54(23–26):2578–2598. <https://doi.org/10.1016/j.dsr2.2007.08.018>
- Chapman CC, Lea MA, Meyer A, Sallée JB, Hindell M (2020) Defining southern Ocean fronts and their influence on biological and physical processes in a changing climate. *Nat Clim Change* 10(3):209–219. <https://doi.org/10.1038/s41558-020-0705-4>
- Deacon G (1937) The hydrography of the southern Ocean. *Discov Rep* 15:1–124
- Donohue KA, Tracey KL, Watts DR, Chidichimo MP, Chereskin TK (2016) Mean Antarctic circumpolar current transport measured in drake passage. *Geophys Res Lett* 43(22):11760–11767. <https://doi.org/10.1002/2016GL070319>
- Downes SM, Langlais C, Brook JP, Spence P (2017) Regional impacts of the westerly winds on southern Ocean mode and intermediate water subduction. *J Phys Oceanogr* 47(10):2521–2530. <https://doi.org/10.1175/JPO-D-17-0106.1>
- Eyring V, Bony S, Meehl GA, Senior CA, Stevens B, Stouffer RJ, Taylor KE (2016) Overview of the coupled model intercomparison project phase 6 (CMIP6) experimental design and organization. *Geosci Model Dev*. <https://doi.org/10.5194/gmd-9-1937-2016>
- Gaspar P, Grégoris Y, Lefevre J-M (1990) A simple eddy kinetic energy model for simulations of the oceanic vertical mixing: tests at station papa and long-term upper ocean study site. *J Geophys Res* 95(C9):16179. <https://doi.org/10.1029/jc095ic09p16179>
- Gent PR, Willebrand J, McDougall TJ, McWilliams JC (1995) Parameterizing Eddy-induced tracer transports in ocean circulation models. *J Phys Oceanogr* 25(4):463–474. [https://doi.org/10.1175/1520-0485\(1995\)025%3c0463:peitti%3e2.0.co;2](https://doi.org/10.1175/1520-0485(1995)025%3c0463:peitti%3e2.0.co;2)
- Gille ST (2003) Float observations of the southern ocean. Part II: Eddy fluxes
- Graham RM, de Boer AM, Heywood KJ, Chapman MR, Stevens DP (2012) Southern Ocean fronts: controlled by wind or topography? *J Geophys Res Oceans*. <https://doi.org/10.1029/2012JC007887>
- Held IM, Larichev VD (1996) A scaling theory for horizontally homogeneous, baroclinically unstable flow on a beta plane. *J Atmos Sci* 53(7):946–963. [https://doi.org/10.1175/1520-0469\(1996\)053%3c0946:astfhh%3e2.0.co;2](https://doi.org/10.1175/1520-0469(1996)053%3c0946:astfhh%3e2.0.co;2)
- Howe N, Czaja A (2009) A new climatology of air–sea density fluxes and surface water mass transformation rates constrained by

- WOCE. *J Phys Oceanogr* 39(6):1432–1447. <https://doi.org/10.1175/2008JPO4025.1>
- Kuhlbrodt T, Jones CG, Sellar A, Storkey D, Blockley E, Stringer M, Hill R et al (2018) The low-resolution version of HadGEM3 GC31: development and evaluation for global climate. *J Adv Model Earth Syst* 10(11):2865–2888. <https://doi.org/10.1029/2018MS001370>
- Langlais CE, Rintoul SR, Zika JD (2015) Sensitivity of Antarctic circumpolar current transport and eddy activity to wind patterns in the southern Ocean. *J Phys Oceanogr* 45(4):1051–1067. <https://doi.org/10.1175/JPO-D-14-0053.1>
- Lin X, Zhai X, Wang Z, Munday DR (2018) Mean, variability, and trend of southern ocean wind stress: role of wind fluctuations. *J Clim* 31(9):3557–3573. <https://doi.org/10.1175/JCLI-D-17-0481.1>
- McCarthy GD, King BA, Cipollini P, McDonagh EL, Blundell JR, Biastoch A (2012) On the sub-decadal variability of south Atlantic Antarctic intermediate water. *Geophys Res Lett* 39(10):1–5. <https://doi.org/10.1029/2012GL051270>
- Meijers AJS (2014) The southern ocean in the coupled model intercomparison project phase 5. *Philos Trans R Soc A Math Phys Eng Sci*. <https://doi.org/10.1098/rsta.2013.0296>
- Meijers AJS, Shuckburgh E, Bruneau N, Sallee JB, Bracegirdle TJ, Wang Z (2012) Representation of the Antarctic circumpolar current in the CMIP5 climate models and future changes under warming scenarios. *J Geophys Res Oceans* 117(12):1–19. <https://doi.org/10.1029/2012JC008412>
- Noh KM, Lim HG, Kug JS (2021) Zonally asymmetric phytoplankton response to the southern annular mode in the marginal sea of the southern ocean. *Sci Rep* 11(1):10266. <https://doi.org/10.1038/s41598-021-89720-4>
- O’neill BC, Tebaldi C, Van Vuuren DP, Eyring V, Friedlingstein P, Hurtt G, Knutti R et al (2016) The scenario model intercomparison project (ScenarioMIP) for CMIP6. *Geosci Model Dev* 9:3461–3482. <https://doi.org/10.5194/gmd-9-3461-2016>
- Orsi AH, Whitworth T, Nowlin WD (1995) On the meridional extent and fronts of the Antarctic circumpolar current. *Deep-Sea Res Part I* 42(5):641–673. [https://doi.org/10.1016/0967-0637\(95\)00021-W](https://doi.org/10.1016/0967-0637(95)00021-W)
- Panassa E, Magdalena Santana-Casiano J, González-Dávila M, Hoppema M, van Steven MAC, Heuven CV, Wolf-Gladrow D, Hauck J (2018) Variability of nutrients and carbon dioxide in the antarctic intermediate water between 1990 and 2014. *Ocean Dyn* 68(3):295–308. <https://doi.org/10.1007/s10236-018-1131-2>
- Piola AR, Gordon AL (1989) Intermediate waters in the Southwest South Atlantic. *Deep-Sea Res* 36:1–16
- Pollard RT, Lucas MI, Read JF (2002) Physical controls on biogeochemical zonation in the southern Ocean. *Deep-Sea Res Part II: Top Stud Oceanogr* 49(16):3289–3305. [https://doi.org/10.1016/S0967-0645\(02\)00084-X](https://doi.org/10.1016/S0967-0645(02)00084-X)
- Portela E, Kolodziejczyk N, Maes C, Thierry V (2020) Interior water-mass variability in the southern hemisphere oceans during the last decade. *J Phys Oceanogr* 50(2):361–381. <https://doi.org/10.1175/JPO-D-19-0128.1>
- Sabine CL, Feely RA, Gruber N, Key RM, Lee K, Bullister JL, Wanninkhof R et al (2004) The oceanic sink for anthropogenic CO<sub>2</sub>. *Science* 305(5682):367–371. <https://doi.org/10.1126/SCIENCE.1097403>
- Sallée J-B, Shuckburgh E, Bruneau N, Meijers AJS, Bracegirdle TJ, Wang Z (2013a) Assessment of southern ocean mixed-layer depths in CMIP5 models: historical bias and forcing response. *J Geophys Res Oceans* 118(4):1845–1862. <https://doi.org/10.1002/jgrc.20157>
- Sallée JB, Shuckburgh E, Bruneau N, Meijers AJS, Bracegirdle TJ, Wang Z, Roy T (2013b) Assessment of southern ocean water mass circulation and characteristics in CMIP5 models: historical bias and forcing response. *J Geophys Res Oceans* 118(4):1830–1844. <https://doi.org/10.1002/jgrc.20135>
- Schmidtko S, Johnson GC, Lyman JM (2013) MIMOC: a global monthly isopycnal upper-ocean climatology with mixed layers. *J Geophys Res-Oceans* 13:1658–1672
- Schmitz WJ, McCartney MS (1993) On the north Atlantic circulation. *Rev Geophys*. <https://doi.org/10.1029/92RG02583>
- Schneider W (2003) Characteristics and formation of eastern south Pacific intermediate water. *Geophys Res Lett* 30(11):1581. <https://doi.org/10.1029/2003GL017086>
- Schouten MW, Matano RP (2006) Formation and pathways of intermediate water in the parallel ocean circulation model’s southern ocean. *J Geophys Res* 111:6015. <https://doi.org/10.1029/2004JC002357>
- Schulzweida U (2019) CDO User Guide (Version 1.9.8). <https://doi.org/10.5281/zenodo.3539275>
- Sellar AA, Jones CG, Mulcahy JP, Tang Y, Yool A, Wiltshire A, O’Connor FM et al (2019) UKESM1: description and evaluation of the UK earth system model. *J Adv Model Earth Syst* 11(12):4513–4558. <https://doi.org/10.1029/2019MS001739>
- Sloyan BM, Kamenkovich IV (2007) Simulation of Subantarctic mode Ana Antarctic intermediate waters in climate models. *J Clim* 20(20):5061–5080. <https://doi.org/10.1175/JCLI4295.1>
- Sloyan BM, Rintoul SR (2001) Circulation, renewal, and modification of Antarctic mode and intermediate water\*
- Sørensen JVT, Ribbe J, Shaffer G (2001) Antarctic intermediate water mass formation in ocean general circulation models
- Speer K, Tziperman E (1992) Rates of water mass formation in the north Atlantic ocean. *J Phys Oceanogr*. [https://doi.org/10.1175/1520-0485\(1992\)022%3c0093:ROWMF1%3e2.0.CO;2](https://doi.org/10.1175/1520-0485(1992)022%3c0093:ROWMF1%3e2.0.CO;2)
- Talley LD (1999) Some aspects of ocean heat transport by the shallow, intermediate and deep overturning circulations. *Geophys Monogr Ser* 112:1–22. <https://doi.org/10.1029/GM112P0001>
- Talley LD, Pickard GL, Emery WJ, Swift JH (2011) Global circulation and water properties. *Descr Phys Oceanogr*. <https://doi.org/10.1016/b978-0-7506-4552-2.10014-9>
- Tang Y, Rumbold S, Ellis R, Kelley D, Mulcahy J, Sellar A, Walton J, Jones C (2019) MOHC UKESM1.0-LL model output prepared for CMIP6 CMIP. *Earth Syst Grid Fed*. <https://doi.org/10.22033/ESGF/CMIP6.1569>
- Treguier AM, England M, Rintoul SR, Madec G, Le Sommer J, Molines J-M (2007) Southern ocean overturning across streamlines in an eddy simulation of the antarctic circumpolar current. *Ocean Sci Discuss* 4(4):653–698. <https://doi.org/10.5194/osd-4-653-2007>
- Walín G (1982) On the relation between sea-surface heat flow and thermal circulation in the ocean. *Tellus* 34(2):187–195. <https://doi.org/10.1111/j.2153-3490.1982.tb01806.x>
- Williams RG, Follows MJ (2011) Ocean dynamics and the carbon cycle. *Ocean dynamics and the carbon cycle*. Cambridge University Press. <https://doi.org/10.1017/cbo9780511977817>
- Williams RG, Marshall JC, Spall MA (1995) Does Stommel’s mixed layer? Demon? Work? *J Phys Oceanogr* 25(12):3089–3102. [https://doi.org/10.1175/1520-0485\(1995\)025%3c3089:DSMLW%3e2.0.CO;2](https://doi.org/10.1175/1520-0485(1995)025%3c3089:DSMLW%3e2.0.CO;2)
- Williams KD, Copsey D, Blockley EW, Bodas-Salcedo A, Calvert D, Comer R, Davis P et al (2018) The met office global coupled model 3.0 and 3.1 (GC3.0 and GC3.1) configurations. *J Adv Model Earth Syst* 10(2):357–380. <https://doi.org/10.1002/2017M001115>
- Yao W, Shi J, Zhao X (2017) Freshening of Antarctic intermediate water in the south Atlantic ocean in 2005–2014. *Ocean Sci* 13(4):521–530. <https://doi.org/10.5194/os-13-521-2017>
- You Y (2002) Dianeutral exchange between intermediate and deep water in the tropical Atlantic. *J Geophys Res*. <https://doi.org/10.1029/2000jc000520>

Zhu C, Liu Z, Sifan Gu (2018) Model bias for south atlantic antarctic intermediate water in CMIP5. *Clim Dyn* 50(9–10):3613–3624. <https://doi.org/10.1007/s00382-017-3828-1>

**Publisher's Note** Springer Nature remains neutral with regard to jurisdictional claims in published maps and institutional affiliations.